Comput Visual Sci 5: 13–34 (2002)
Digital Object Identifier (DOI) 10.1007/s00791-002-0084-6

Computing and
Visualization in Science
© Springer-Verlag 2002

Regular article

A framework for computational anatomy

Paul M. Thompson, Arthur W. Toga

Laboratory of Neuro Imaging, Dept. of Neurology, Division of Brain Mapping, UCLA School of Medicine, Los Angeles, CA 90095, USA
(e-mail: thompson@loni.ucla.edu)

Received: 13 August 2001

Communicated by: C. Johnson and M. Rumpf

Abstract. The rapid collection of brain images from healthy and diseased subjects has stimulated the development of powerful mathematical algorithms to compare, pool and average brain data across whole populations. Brain structure is so complex and variable that new approaches in computer vision, partial differential equations, and statistical field theory are being formulated to detect and visualize disease-specific patterns. We present some novel mathematical strategies for computational anatomy, focusing on the creation of population-based brain atlases. These atlases describe how the brain varies with age, gender, genetics, and over time. We review applications in Alzheimer's disease, schizophrenia and brain development, outlining some current challenges in the field.

1 Diversity of brain maps

Recent developments in brain imaging have greatly empowered medicine and neuroscience. The ability to image the structure and function of the living brain has also accelerated the collection and databasing of brain maps. These maps store information on anatomy and physiology, from whole-brain to molecular scales, some capturing dynamic changes that occur over milliseconds or even over entire lifetimes (see e.g. Toga and Mazziotta 1996; Frackowiak et al. 1997, for recent reviews).

Since the development of computerized tomography (CT; Hounsfield 1973) and magnetic resonance imaging techniques (Lauterbur 1973), maps of brain structure have typically been based upon 3D tomographic images (Damasio 1995). Angiographic or spiral CT techniques can also visualize vascular anatomy (Fishman 1997), while diffusion tensor images can even reveal fiber topography in vivo (Turner et al. 1991; Mori et al. 2001; Jacobs and Fraser 1994). These brain maps can be supplemented with high-resolution information from anatomic specimens (Talairach and Tournoux 1988; Ono et al. 1990; Duvernoy 1991) and a variety of histologic preparations which reveal regional cytoarchitecture (Brodmann 1909) and regional molecular content such as myelination patterns (Smith 1907; Mai et al. 1997), receptor binding sites (Geyer et al. 1997), protein densities and mRNA distributions. Other brain maps have concentrated on function, quantified by positron emission tomography (PET; Minoshima et al. 1994), functional MRI (Le Bihan 1996), electrophysiology (Avoli et al. 1991; Palovcik et al. 1992) or optical imaging (Cannestra et al. 1996). Additional maps have been developed to represent neuronal connectivity and circuitry (Van Essen and Maunsell 1983), based on compilations of empirical evidence (Brodmann 1909; Berger 1929; Penfield and Boldrey 1937).

Despite the diversity of brain maps, each has a different spatial scale and resolution, emphasizes different functional or structural characteristics, and none is inherently compatible with any other. Each strategy clearly has its place within a collective effort to map the brain, but unless certain precautions are taken (enabling common registration), these brain maps will remain as individual and independent efforts, and the correlative potential of the many diverse mapping approaches will be underexploited.

Anatomical variability

A further computational problem arises when integrating and comparing brain data. Brain structure is so complex, and varies so markedly across subjects, that it is difficult to compare one brain image with another, or integrate them in a common reference space. To tackle these problems, many laboratories are using sophisticated engineering approaches drawn from computer vision, image analysis, computer graphics and artificial intelligence research fields to manipulate, analyze and communicate brain data. A major goal of these studies is to analyze how the dynamically changing brain varies across age, gender, disease, across multiple imaging modalities, and in large human populations (Mazziotta et al. 1995, 2001; Collins et al. 1995; Giedd et al. 1999; Ashburner et al. 1999). Efforts to uncover new patterns of altered structure and function in individuals and clinical populations have

also led to the new field of *computational anatomy* (Grenander and Miller 1998; Thompson et al. 2001; Fischl et al. 1999; Davatzikos et al. 1996; Bookstein 2001). This growing field has powerful applications in neuroscience, uncovering, for example, how the brain grows in childhood (Thompson et al. 2000), how genes affect brain structure (Thompson et al. 2001; Cannon et al. 2001; Styner and Gerig 2001), and how diseases such as Alzheimer's, schizophrenia, or multiple sclerosis evolve over time or respond to therapy (Freeborough and Fox 1998; Subsol et al. 1997; Zijdenbos et al. 1996; Thompson et al. 2001; Haney et al. 2001). As imaging databases have expanded, disease-specific patterns of brain structure can now be detected (Thompson et al. 1997, 2001; Csernansky et al. 1998), as well as group patterns of brain organization that are not apparent in an individual subject (Narr et al. 2001). The resulting algorithms are receiving growing interest in the neuroscience community, where they are being applied primarily to uncover new aspects of brain development and disease (Giedd et al. 1999; Sowell et al. 1999; Sowell et al. 2001; Paus et al. 1999; Thompson et al. 2000, 2001).

2 Brain atlases: from individuals to populations

To address the difficulties in comparing brain maps, **brain atlases** (e.g. Talairach and Tournoux 1988; Swanson 1992; Evans et al. 1994; Mazziotta et al. 1995; Spitzer et al. 1996; Kikinis et al. 1996; Drury and Van Essen 1997; Schmahmann et al. 2001) provide a structural framework in which individual brain maps can be integrated. Most brain atlases are based on a detailed representation of a single subject's anatomy in a standardized 3D coordinate system, or stereotaxic space. The chosen data set acts as a template on which other brain maps (such as functional images) can be overlaid. The anatomic data provides the additional detail necessary

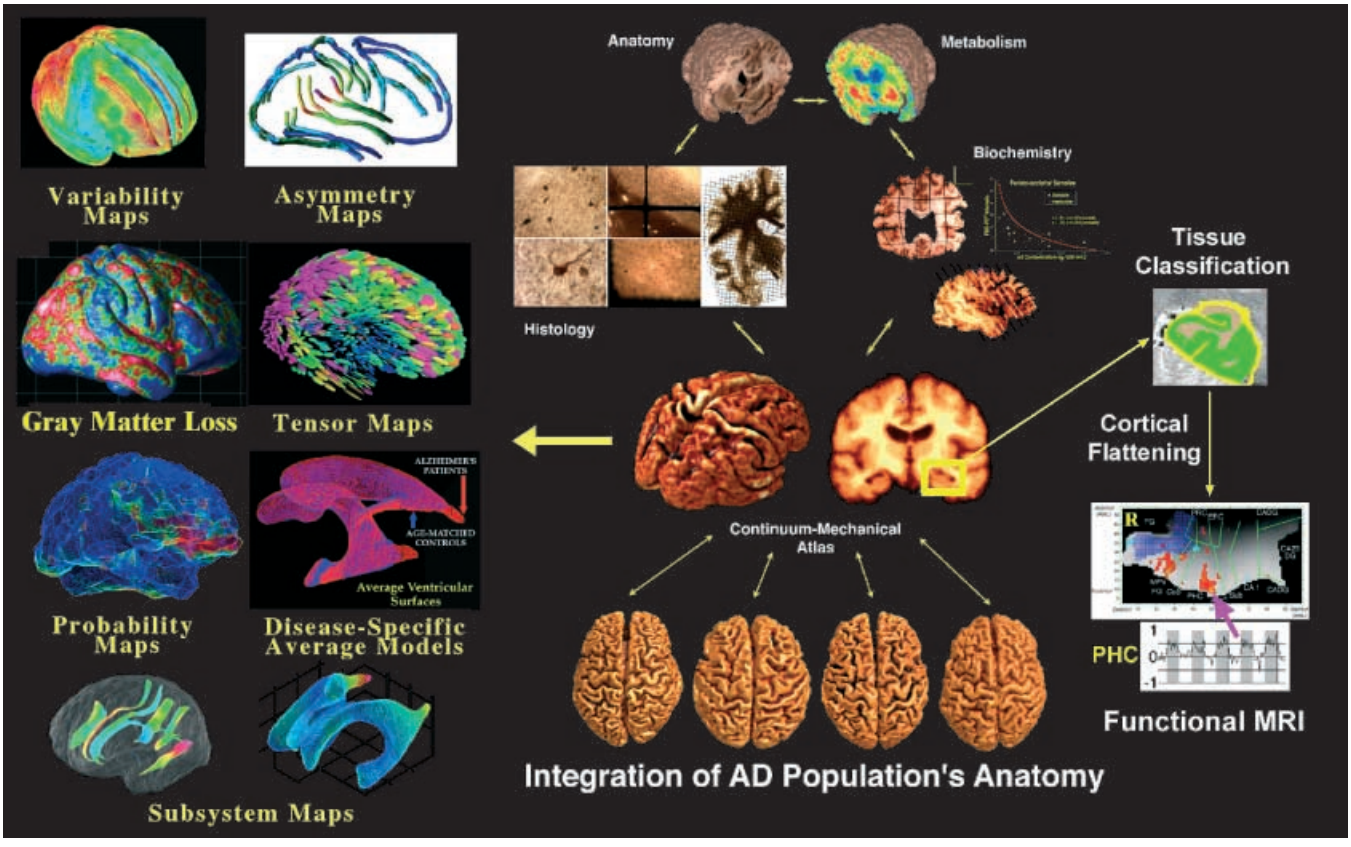

Fig. 1. Elements of a disease-specific atlas. This schematic shows the types of maps and models contained in a disease-specific brain atlas (Thompson et al. 2000; Mega et al. 2000). A diverse range of computational anatomical tools are required to generate these average brain image templates (continuum-mechanical atlas), models and maps. Disease-specific brain atlases, such as this one based on patients with Alzheimer's disease (AD), allow imaging data from diverse modalities to be compared and correlated in a common 3D coordinate space. 3D anatomical models (e.g. cortical surfaces, *bottom row*), were extracted from a database of structural MRI data from AD patients. Models of these and other structures were digitally averaged and used to synthesize an average brain template (continuum-mechanical atlas, *middle*) with well-resolved anatomical features in the mean shape and size for the population (see Thompson et al. 2001 for details). By rotating and scaling new images to occupy the same space as this template, models of subcortical, ventricular and deep nuclear structures can be built (*lower left*). Average models for patients and controls then be used to compute average patterns and statistics of cortical variability and asymmetry (*top left*), to chart average profiles of gray matter loss in a group (see Fig. 9), and to detect atrophy in a group or individual (*probability maps; left column*). Mega et al. (1997, 1999) also fused histologic maps of *post mortem* neurofibrillary tangle (NFT) staining density, biochemical maps of beta-amyloid distribution, and 3D metabolic FDG-PET data obtained 8 h before death, in the same patient with AD (*top middle panels*). By classifying gray and white matter (tissue classification) and unfolding the topography of the hippocampus (*right panels*), Zeineh et al. (2001) revealed the fine-scale anatomy and dynamics of brain activation during memory tasks, using high-resolution functional MRI (time course shown for activation in right parahippocampal cortex, PHC). Atlasing techniques can represent and compare these diverse datasets in a common coordinate space, enabling novel multi-subject and cross-modality comparisons

to accurately localize activation sites, as well as providing other structural perspectives such as chemoarchitecture. Digital mapping of structural and functional image data into a common 3D coordinate space is a prerequisite for many types of brain imaging research, as it supplies a quantitative spatial reference system in which brain data from multiple subjects and modalities can be compared and correlated.

Given the fact that there is neither a single representative brain nor a simple method to construct an "average" anatomy or represent the complex variations around it, the construction of brain atlases to represent large human populations has become the focus of intense research. Recent advances in morphometry have also allowed the detection of structural patterns associated with specific diseases (Csernansky et al. 1998; Thompson et al. 2001), genetic risk factors (Cannon et al. 2001), heredity (Thompson et al. 2001), and therapeutic response in large populations (e.g. Thompson et al. 2001; see Mazziotta et al. 2001). Deformable atlases (Bohm et al. 1983; Miller et al. 1993; Collins et al. 1995; Rizzo et al. 1995; Thompson et al. 2001a,b), which can be adapted to reflect the anatomy of new subjects, and probabilistic atlases (Mazziotta et al. 1995), which retain information on population variability, can be used to guide knowledge-based image analysis algorithms, and can even support pathology detection in individual subjects or groups (Thompson et al. 1997). Multi-modality atlases combine detailed structural maps from multiple imaging sensors in the same 3D coordinate space (e.g. Cannestra et al. 1998). These atlases provide the best of all worlds, offering a realistically complex representation of brain morphology and function in its full spatial and multidimensional complexity. Disease-specific atlases (Mega et al. 2000; Thompson et al. 2000) are also powerful research tools that provide a unique view of a particular disease. They can integrate maps from histologic, biochemical, and metabolic projects with structural images, templates and models derived from a population of patients (Fig. 1). While such atlases relate the anatomic and histopathological underpinnings to in vivo metabolic and perfusion maps of this disease, a realistically complex algorithmic framework is required to bring new data into the atlas and discover structural and functional patterns in these large databases (Megalooikonomou et al. 2000).

Deformable brain templates

A major focus in computational anatomy has been the development of *image warping algorithms*. These elastically re-shape a brain atlas to match the anatomy of new individuals (see Toga 1998 for a review). The transforms that map an atlas onto a large number of individuals also provide a rich source of morphometric data for data mining or hypothesis testing. The algorithms, in turn, have capitalized on fundamental work in computer vision, particularly on deformable templates. In a deformable template approach, shapes evolve in an image to segment or label objects (Kass et al. 1987; Sapiro 2001). Statistics on the deformation parameters may also be estimated to encode shape variability for pattern recognition or statistical inference (Cootes et al. 1995; Grenander and Miller 1994). The resulting *deformable brain atlases* can project detailed atlas data into new scans, including maps of cytoarchitecture, biochemistry, functional and vascular territories. Their uses include surgical planning (Warfield et al. 1998; St-Jean et al. 1998), anatomical labeling (Iosifescu et al. 1997) and shape measurement (Subsol 1995; Thompson et al. 1997; Haller et al. 1997; Csernansky et al. 1998). The shape of the digital atlas is adapted using local warping transformations (dilations, contractions and shearing), producing an *individualized* brain atlas (Fig. 2). These transformations allow any segment of the atlas anatomy, however small, to grow, shrink, twist and even rotate, producing a transformation that encodes local differences in topography from one individual to another. The ability to automatically map labeled brain atlases onto individual scans has many applications. Digital anatomic models can be projected into PET data to define regions of interest for quantitative calculations of regional cerebral blood flow (Ingvar et al. 1994; Dinov et al. 2000). Brain structures can also be labeled for hippocampal morphometry in dementia (Haller et al. 1997), for analysis of subcortical structure volumes in schizophrenia (Iosifescu et al. 1997; Csernansky et al. 1998; Gaser et al. 1998), for estimation of structural variation and pathology detection (Collins et al. 1994; Thompson et al. 1997), and for segmentation and classification of multiple sclerosis lesions (Warfield et al. 1995).

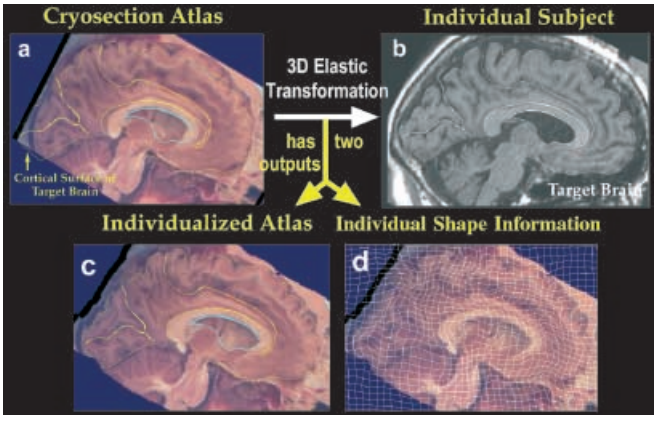

Fig. 2a–d. Computing anatomical differences with a deformable brain atlas. When a cryosection atlas of the brain (**a**) is deformed to match the anatomy of an individual patient (**b**), here imaged with 3D MRI, there are two useful products. The first is an high-resolution anatomical template that is customized to reflect the individual's anatomy, and the second is a mathematical record of the shape differences between the atlas and the individual (*warped grid*, (**d**)). These fields can be analyzed statistically to quantify differences in brain structure and detect abnormal anatomy. The transformation of the atlas onto the target MRI is here performed by constraining functionally important surfaces to match, while extending the deformation to the full 3D volume (Thompson and Toga 1996)

Deformation-based morphometry

In view of its broad applications, non-linear registration has a fundamental role in image analysis. Considerable ingenuity has therefore gone into designing algorithms that use both anatomic and mathematical criteria to reconfigure one anatomy onto another. Since many developmental and disease processes (e.g. dementia and schizophrenia) alter anatomy in a systematic way, the deformations mapping an anatomic template onto a population of subjects can be analyzed to detect subtle differences in brain structure. While shape variation is not the only index of disease or anatomical difference available in an image (image intensity or other morphometric measures may be used as well), shape differences are often

powerful descriptors of disease (Bookstein 1997). Automated recovery of deformation maps from a large image database therefore provides extraordinary potential for detecting genetic and therapeutic effects on brain structure (Guimond et al. 1999; Thompson et al. 2001). Because of their relevance to computational anatomy, some background information on warping algorithms is given next. Their strengths are outlined, prior to introducing a more comprehensive anatomical modeling approach which accommodates the most variable, and most highly studied, of brain structures – the cerebral cortex (Sect. 4).

3 Warping algorithms

Non-linear registration approaches are commonly classified into two major types, *intensity-based* and *model-based*, depending on the type of information that drives them (see Toga 1998, for a review). *Model-driven* algorithms first build explicit geometric models, representing separate, identifiable anatomic elements in each of the scans to be matched. These anatomical systems typically include functionally important surfaces (Szeliski and Lavallée 1993; Downs et al. 1994; Moshfeghi et al. 1995; Thompson and Toga 1996; Davatzikos 1996), curves (Ge et al. 1995; Monga and Benayoun 1995; Subsol 1995), and point landmarks (Bookstein 1989; Amit et al. 1997). Anatomical elements are parameterized and matched with their counterparts in the target scan, and their correspondences guide the volumetric transformation of one brain to another. In our own warping algorithms (Fig. 2; Thompson and Toga 1996, 2001), higher-level structural information guides the mapping of one brain onto another, and a hierarchy of curve-to-curve and surface-to-surface mappings is set up, guaranteeing the gross anatomical validity of the resulting transform. Anatomical information is used to match cortical regions, so that networks of sulci and gyri are individually matched. These strategies are discussed in Sect. 4. First, however, simpler deformation approaches are reviewed as they provide a rich source of anatomic information.

Intensity-driven approaches

Intensity-driven approaches for image warping aim to match regional intensity patterns in each scan based on mathematical or statistical criteria. Typically, they define a mathematical measure of intensity similarity between the deforming scan and the target. Measures of intensity similarity can include squared differences in pixel intensities (Woods et al. 1993, 1998; Christensen et al. 1993; Ashburner et al. 1997), regional correlation (Bajcsy and Kovacic 1989; Collins et al. 1995), or mutual information (Kim et al. 1997). Mutual information has proved to be an excellent similarity measure for *cross-modality* registrations. It assumes only that the *statistical dependence* of the voxel intensities is maximal when the images are geometrically aligned (Wells et al. 1997; Viola and Wells 1995; Sarrut 2000)[1]. The intensity similarity measure, often combined with a measure of the structural integrity of the deforming scan, is optimized by adjusting parameters of the deformation field.

The widely-used *Automated Image Registration* (AIR; Woods et al. 1998) and *Statistical Parametric Mapping* algorithms (Ashburner and Friston 1999) are examples of registration approaches that can measure (or, in other contexts, *factor out*) anatomical differences, using warping fields. As the cost function (or *similarity measure*) is optimized, increasingly complex warping fields are expressed in terms of a 3D cosine basis (SPM) or by tuning parameters of 3D polynomials (AIR). These fields contain increasing amounts of information on anatomic differences between an individual and an atlas, which is successively deformed to match them. In SPM, the target image $g(\boldsymbol{x})$ is approximated by a scaled (by factor w) and spatially deformed version of the individual's image $f(\boldsymbol{x})$. The deformation is constrained to be a linear combination of smooth basis functions:

$$\boldsymbol{u}(\boldsymbol{x}) = \left[\sum_j t_{j,1} b_{1,j}(\boldsymbol{x}), \sum_j t_{j,2} b_{2,j}(\boldsymbol{x}), \sum_j t_{j,3} b_{3,j}(\boldsymbol{x}) \right] , \tag{1}$$

where $b_{d,j}(\boldsymbol{x})$ is the jth-order basis function along axis d at position $\boldsymbol{x}$. The coefficients $t_{j,d}$ of the deformation field can be assembled, with the intensity scale-factor, into a parameter vector, $\boldsymbol{p} = \left[\boldsymbol{t}_x \boldsymbol{t}_y \boldsymbol{t}_z w\right]$ and their values can be chosen to minimize the least-squares cost function:

$$\sum_i \left[C\left(\boldsymbol{x}_i, \boldsymbol{p}\right)\right]^2 = \sum_i \left[f(\boldsymbol{y}_i) - w g(\boldsymbol{x}_i)\right]^2 , \tag{2}$$

where $\boldsymbol{y}_i$ is the displaced position of the ith voxel $\boldsymbol{y}_i = \boldsymbol{x}_i - \boldsymbol{u}(\boldsymbol{x}_i)$. To optimize the deformation, note that a small increment $\boldsymbol{t}$ in the parameter vector will affect the cost function at each voxel i according to the first-order Taylor approximation:

$$C_i\left(\boldsymbol{x}_i, \boldsymbol{p}+\boldsymbol{t}\right) \cong C_i\left(\boldsymbol{x}_i, \boldsymbol{p}\right) + t_1 \left[\partial C_i\left(\boldsymbol{x}_i, \boldsymbol{p}\right) \big/ \partial p_i\right] + t_2 \left[\partial C_i\left(\boldsymbol{x}_i, \boldsymbol{p}\right) \big/ \partial p_2\right] + \ldots \tag{3}$$

At a global (or local) minimum of the cost function, $\sum_i \left[C(\boldsymbol{x}_i,\ \boldsymbol{p}+\boldsymbol{t})\right]^2$, a linear system $\boldsymbol{A}\boldsymbol{t} \cong \boldsymbol{b}$ can be written down and solved for the parameter increment $\boldsymbol{t}$. Here the matrix elements $\boldsymbol{A}_{rs} = [\partial C_r(\boldsymbol{x}_r, \boldsymbol{p}) / \partial p_s]$ are computed from the image gradients (using the chain rule), and $\boldsymbol{t} = [t_1, t_2, \ldots]^{\mathrm{T}}$ and $\boldsymbol{b} = [C_1(\boldsymbol{p}), C_2(\boldsymbol{p}), \ldots]^{\mathrm{T}}$. To find the optimal parameters, the deforming image is resampled at each iteration n, and the parameters $\boldsymbol{p}$ are updated using the Gauss–Newton rule:

$$\boldsymbol{p}^{(n+1)} = \boldsymbol{p}^{(n)} - \left(\boldsymbol{A}^{\mathrm{T}}\boldsymbol{A}\right)^{-1} \boldsymbol{A}^{\mathrm{T}}\boldsymbol{b} , \tag{4}$$

[1] The idea of mutual information-based registration is to deform an image S until the mutual information (MI) between it and the target image T is maximized (Kim et al. 1997; Maintz and Viergever 1998). A joint probability distribution $p(s,t)$ is estimated by binning the image intensity pairs for voxels in the overlapping part of the images. This distribution is compared with the probability distribution $p(s)\,p(t)$ that would randomly arise if the images were scrambled relative to each other (independent). The *Kullback–Leibler divergence* (or *relative entropy*) measures how different these two probability distributions are, and quantifies the mutual information between the two images. Other information-theoretic measures, such as the Rényi entropy or Toussaint's divergence (Sarrut 2000) may offer even more accurate and robust image matching in some applications, and are under investigation for image data mining applications.

until the cost function is minimized. Ashburner and Friston (1999) accelerated this scheme by simplifying the large curvature matrix $\boldsymbol{A}^{\mathrm{T}}\boldsymbol{A}$ using known identities for Kronecker tensor products. They also added a Bayesian regularization term to pull parameter estimates towards their expected values, avoiding unnecessary deformations and accelerating convergence. As in other Bayesian approaches, this covariance term was derived analytically by assuming a Gibbs statistical prior distribution on the deformation energies (cf. Miller et al. 1993). The deformation energy $E(\boldsymbol{p})$, computed from the transformation parameters, can be transformed into a Gibbs (or Boltzmann) distribution on the expected deformations:

$$P(\boldsymbol{p}) = (1/Z)\exp\left[-E(\boldsymbol{p})\right] . \tag{5}$$

Here Z is the partition function that normalizes the distribution. In the SPM approach, the covariance matrix of the deformation parameters is expanded in terms of the eigenfunctions of the governing operator (here the DCT basis functions), and used to add a Bayesian prior term that pulls the mapping away from unrealistic deformations. In a further innovation, Gee and Le Briquer (1997) recovered deformations that were most 'brain-like' by deriving from a set of inter-subject mappings, $\boldsymbol{u}^{(i)}(\boldsymbol{x})$, a new orthogonal basis on the deformation space by Gram–Schmidt orthogonalization of the deformation fields (cf. related approaches in face recognition based on eigenmodes of variation; Turk and Pentland 1991). In new basis, the mean and covariance matrix of the deformation coefficients specified a Gaussian prior on the deformation space. A linear system was then solved for the mapping that optimizes a combination of least-squares intensity similarity and prior probability, as quantified by the empirical distribution. As the principal components (modes) of deformation are computed in advance, the resulting mappings are computed rapidly, guided by empirical knowledge on brain shape variability (cf. Ashburner et al. 1997; Wang and Staib 1998, for related approaches).

Probabilistic measures of anatomic variation

Even the lowest order deformations contain substantial information on morphometric differences among subjects. Without higher order anatomic information to enforce the correct anatomic correspondences, the purely intensity-based registration measures often match structures that do not correspond anatomically, especially at the cortex. So depending on the goals of the study, these algorithms can either be used in isolation, or prior to computing higher-order mappings or extracting anatomical models, as described in the next sections. By defining probability distributions on the space of deformation transformations that drive the anatomy of different subjects into correspondence (Grenander 1976; Amit et al. 1991; Grenander and Miller 1994; Thompson and Toga 1997; Thompson et al. 1997), statistical parameters of these distributions can be estimated from databased anatomic data. The magnitude and directional biases of anatomic variation can then be estimated. Encoding of local variation can be used to assess the severity of structural variants outside of the normal range, which, in brain data, may be a sign of disease (Thompson et al. 1997).

Detecting brain structure differences

For analyzing the extremely complex anatomical deformation maps described later, with millions of degrees of freedom, random field methods have been advocated (Thompson et al. 1996, 1997, 2001; Cao and Worsley 2001; Worsley et al. 1999; Bullmore et al. 1999; Younes and Miller 2001; see Sect. 4). Deformations represented by a small set of basis functions can be analyzed by spectral methods. In Grenander's formalism (Grenander and Miller 1998; Joshi et al. 1995), the distribution of the random deformation fields $\boldsymbol{u}(\boldsymbol{x})$ is assumed to satisfy the stochastic differential equation:

$$L\left(\boldsymbol{u}(\boldsymbol{x})\right) = \boldsymbol{e}(\boldsymbol{x}) . \tag{6}$$

Here L is the operator governing the deformation (for more on this, see below; in SPM, this is the Laplacian, whose eigenbasis of sine and cosine functions are used to parameterize the deformation). $\boldsymbol{e}(\boldsymbol{x})$ is a 3×1 random noise vector field, whose coefficients in L's eigenbasis are zero-mean independent Gaussian variables with variances σ_k^2. If the differential operator L has eigenbasis $\{\varphi_k\}$ with eigenvalues $\{\lambda_k\}$, a probability density can be defined directly on the deformation field's expansion coefficients $(z_1, \ldots, z_n)$, grouped into a multivariate vector $\boldsymbol{z}$. If

$$\boldsymbol{u}(\boldsymbol{x}) = \sum_k z_k \varphi_k(\boldsymbol{x}) \tag{7}$$

then:

$$p\left(z_1, \ldots, z_n\right) = \exp -(1/2)\left(\sum_{k=1 \text{ to } n} q \log\left\{2\pi\sigma_k^2 / \lambda_k^2\right\} + \sum_{k=1 \text{ to } n} \left\{|\lambda_k z_k|^2 / \sigma_k^2\right\} \right) . \tag{8}$$

Essentially this spectral formulation is a model of anatomic variability. Once the model parameters σ_k are learned, every subject's anatomy can be represented by a feature vector $(z_1, \ldots, z_n)$, whose elements are just the coefficients of the deformation field required to match their particular anatomy with a mean anatomical template. If the parameters of anatomical variation are altered in disease, a pattern classifier can classify new subjects according to their statistical distance from the diseased group mean relative to the normal group mean (Thompson et al. 1997; Joshi et al. 1998). Martin et al. (1995) proposed a similar approach to assess basal ganglia shape in schizophrenia, using a linear Gaussian classifier, and spatial modes computed either by physical modal analysis (i.e. vibration modes; cf. Brechbühler et al. 1995), or eigenshapes computed by PCA. From a validation standpoint, the classification ability of such a system can be investigated on clinical data (i.e., false positives versus false negatives; Thompson et al. 1997; Joshi et al. 1998).

Statistical models

Multivariate statistics, based on the deformation coefficients, have also been used to compare the gross morphometry of

male and female brains, as well as effects of handedness, and brain asymmetry on brain structure (Ashburner et al. 1999; cf. Bookstein 1997; Thompson et al. 1998, 2001). In Ashburner et al. 1999, a set of deformation mappings was compacted using principal components analysis, producing a set of vectors with new coefficients (20 parameters accounting for 96% of the variance of the estimated mappings). By performing MANCOVA (multivariate analysis of covariance) on these new vectors, effects of confounding factors that might affect brain structure (e.g. age), and even interactions between variables, were quantified or discounted. If the data vectors, covariates of interest, and confounds are represented by matrices $\boldsymbol{A}(m \times n)$, $\boldsymbol{C}(m \times c)$ and $\boldsymbol{G}(m \times g)$, then variance due to the confounds $\boldsymbol{G}$ is eliminated with $\boldsymbol{A}_\mathrm{a} = \boldsymbol{A} - \boldsymbol{G}(\boldsymbol{G}^\mathrm{T}\boldsymbol{G})^{-1}\boldsymbol{G}^\mathrm{T}\boldsymbol{A}$, and the design matrix is orthogonalized with respect to $\boldsymbol{G}$ with $\boldsymbol{C}_\mathrm{a} = \boldsymbol{C} - \boldsymbol{G}(\boldsymbol{G}^\mathrm{T}\boldsymbol{G})^{-1}\boldsymbol{G}^\mathrm{T}\boldsymbol{C}$. The decrease in predictability of the deformations, once the effects of interest are discounted, is measured using the *Wilk's Lambda* statistic (Krzanowski 1988):

$$\Lambda = \det(\boldsymbol{W}) / \det(\boldsymbol{B} + \boldsymbol{W}) ,$$
$$\text{where } \boldsymbol{B} = \boldsymbol{T}^\mathrm{T}\boldsymbol{T} , \quad \boldsymbol{W} = (\boldsymbol{A}_\mathrm{a} - \boldsymbol{T})^\mathrm{T} (\boldsymbol{A}_\mathrm{a} - \boldsymbol{T}) ,$$
$$\boldsymbol{T} = \boldsymbol{C}_\mathrm{a} \left(\left(\boldsymbol{C}_\mathrm{a}^\mathrm{T} \boldsymbol{C}_\mathrm{a} \right)^{-1} \boldsymbol{C}_\mathrm{a}^\mathrm{T} \boldsymbol{A}_\mathrm{a} \right) . \qquad (9)$$

Here Λ has an approximate null distribution of $\exp\left[\chi^2_{\mathrm{nc}} / ((n-c-1)/2-(m-c-g))\right]$, where χ^2_{nc} is a χ^2 statistic with nc degrees of freedom. The results of such analyses are a significance value (p-value) for the effect (e.g. of disease or handedness, on anatomy), and one or more canonical vectors (or deformations that are eigenvectors of the fitted effects, $\boldsymbol{B}$) which caricature the effect (Ashburner et al. 1999). Currently being tested as a framework to encode anatomic variation, these deformable template systems show considerable promise in identifying disease-specific differences (Haller et al. 1997; Joshi et al. 1998; Thompson et al. 2001).

Higher-dimensional anatomical mappings

Both SPM and AIR express deformation fields using global deformation functions. The complexity of the mappings is generally not increased beyond $8 \times 8 \times 8$ basis functions or 8th order polynomial mappings. Physical continuum models, however (Fig. 3), allow extremely flexible deformations, potentially with as many degrees of freedom as there are voxels in the image. These approaches consider the deforming image to be embedded in a 3D elastic or fluid medium. Distributed internal forces reconfigure the image to match the target. These forces can also be based on the local intensity patterns in the datasets, to match image regions of similar intensity.

Elastic and fluid models

In elastic media, the displacement field $\boldsymbol{u}(\boldsymbol{x})$ resulting from internal deformation forces $\boldsymbol{F}(\boldsymbol{x})$ (called *'body forces'*) obeys the Navier–Stokes equilibrium equations for linear elasticity (Bajcsy and Kovacic 1989):

$$\mu \nabla^2 \boldsymbol{u} + (\lambda + \mu) \nabla \left(\nabla^\mathrm{T} \bullet \boldsymbol{u}(\boldsymbol{x}) \right) + \boldsymbol{F}(\boldsymbol{x}) = \boldsymbol{0} , \quad \forall \boldsymbol{x} \in \mathrm{R} . \qquad (10)$$

Here R is a discrete lattice representation of the scan to be transformed, $\nabla^\mathrm{T} \bullet \boldsymbol{u}(\boldsymbol{x}) = \sum \partial u_j / \partial x_j$ is the divergence, or cubical dilation of the medium, ∇^2 is the Laplacian operator, and Lamé's coefficients λ and μ refer to the elastic properties of the medium (see Fig. 3). Body forces, designed to match regions in each dataset with high intensity similarity,

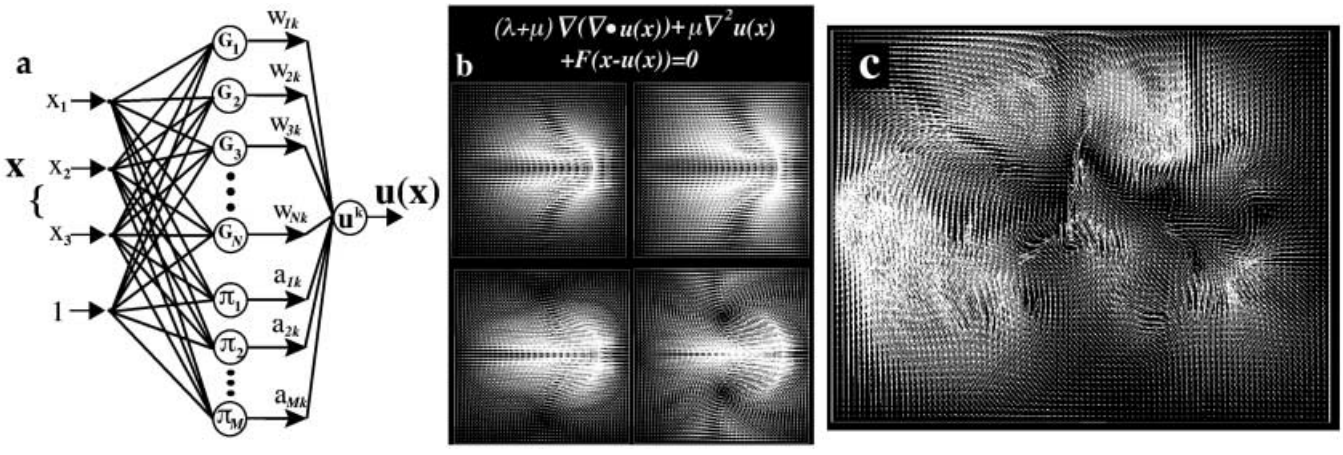

Fig. 3a–c. Deforming anatomical templates with neural nets and continuum mechanical flows. The complex transformation required to reconfigure one brain into the shape of another (Fig. 2) can be determined using neural networks (**a**) or continuum-mechanical models [(**b**),(**c**)], which describe how real physical materials deform. In Davis et al. (1997), each of the 3 deformation vector components, $\boldsymbol{u}^k(\boldsymbol{x})$, is the output of the neural net when the position in the image to be deformed, $\boldsymbol{x}$, is input to the net. Outputs of the hidden units (G_i, π_m) are weighted using synaptic weights, w_{ik}. If landmarks constrain the mapping, the weights are found by solving a linear system. Otherwise, the weights can be tuned so that a measure of similarity between the deforming image and the target image is optimized. Continuum-mechanical models, **(b)**, can also be used to compute these deformation fields. These models describe how real physical materials deform. Different choices of the Lamé elasticity coefficients, λ and μ, in the Cauchy–Navier equations (shown in continuous form, **(b)**) result in different deformations, even if the applied internal displacements are the same. For brain image transformations, values of elasticity coefficients can be chosen to limit the amount of curl (*middle right*) in the deformation field. (*Note*: To help visualize differences, displacement vector fields have been multiplied by a factor of 10, but the elasticity equations are valid only for small deformations). **c** shows the complexity of a typical deformation field, in this case one used to reconfigure a histologic section stained for molecular content. Curve and surface anatomic landmarks are used to constrain the mapping, and the Cauchy–Navier equations are solved to estimate how the rest of the 3D volume deforms. [Panel **a** is adapted from Davis et al. 1997]

can be derived from the gradient of a cost function, such as intensity correlation. Christensen et al. (1993, 1995, 1996) proposed a viscous-fluid based warping transform, motivated by capturing non-linear topological behavior and large image deformations (see also Dupuis et al. 1998; Joshi 1998). Similar to SPM, a low-order deformation is computed first in terms of an approximation series of eigenfunctions of the linear elasticity operator $\mu\nabla^2\boldsymbol{u}+(\lambda+\mu)\nabla(\nabla^{\mathrm{T}}\bullet)$. This basis function representation of the deformation is analogous to the discrete cosine basis used in SPM (which corresponds to the Laplacian operator ∇^2). The elastic eigenfunctions penalize extreme dilation and compression of the deformed image, via an additional gradient-of-the-divergence term $\nabla(\nabla^{\mathrm{T}}\bullet)$ not present in the Laplacian formulation. Basis coefficients are determined by gradient descent on a cost functional (11) that penalizes squared intensity mismatch between the deforming template $T(\boldsymbol{x}-\boldsymbol{u}(\boldsymbol{x},t))$ and target $S(\boldsymbol{x})$:

$$C(T(\boldsymbol{x}),S(\boldsymbol{x}),\boldsymbol{u})=(1/2)\int_{\Omega}\left|T\big(\boldsymbol{x}-\boldsymbol{u}(\boldsymbol{x},t)\big)-S(\boldsymbol{x})\right|^2 d\boldsymbol{x} \quad (11)$$

By contrast with SPM and AIR, stochastic gradient descent is used to find the optimal warping field parameters according to:

$$d\mu_{i,j,r}(t)=-(1/2)\left[\partial H(\boldsymbol{u}(t))\,\big/\,\partial\mu_{i,j,r}\right]dt+dw_{i,j,r}(t)\,. \quad (12)$$

Here $\mu_{i,j,r}(t)$ is the expansion coefficient set for the deformation field in terms of the eigenbasis $\left\{\boldsymbol{e}_{i,j,r}\right\}$ for the linear elasticity operator, $H(\boldsymbol{u}(t))$ is the combined measure of intensity mismatch and deformation severity, and $dw_{i,j,r}(t)$ is a Wiener process allowing parameter estimates to jump out of local minima. At the expense of added computation time, stochastic sampling allows globally optimal image matches to be estimated. Finally, a *viscous* deformation stage allows large-distance, non-linear fluid evolution of the neuroanatomic template. The driving force, which deforms the anatomic template, is defined as the variation of the cost functional with respect to the displacement field:

$$\boldsymbol{F}(\boldsymbol{x},\boldsymbol{u}(\boldsymbol{x},t))=-\left(T(\boldsymbol{x}-\boldsymbol{u}(\boldsymbol{x},t))-S(\boldsymbol{x})\right)\nabla T\big|_{\boldsymbol{x}-\boldsymbol{u}(\boldsymbol{x},t)} \quad (13)$$

$$\mu\nabla^2\boldsymbol{v}(\boldsymbol{x},t)+(\lambda+\mu)\nabla\left(\nabla^{\mathrm{T}}\bullet\boldsymbol{v}(\boldsymbol{x},t)\right)+\boldsymbol{F}(\boldsymbol{x},\boldsymbol{u}(\boldsymbol{x},t))=\boldsymbol{0} \quad (14)$$

$$\partial\boldsymbol{u}(\boldsymbol{x},t)\big/\partial t=\boldsymbol{v}(\boldsymbol{x},t)-\nabla\boldsymbol{u}(\boldsymbol{x},t)\boldsymbol{v}(\boldsymbol{x},t)\,. \quad (15)$$

The deformation velocity (14) is governed by the creeping flow momentum equation for a Newtonian fluid and the conventional displacement field in a Lagrangian reference system (15) is connected to a Eulerian velocity field by the relation of material differentiation. Experimental results were excellent (Christensen et al. 1996).

Acceleration with fast filters

Vast numbers of parameters are required to represent complex deformation fields. In early implementations, deformable registration of a 128^3 MRI atlas to a patient took 9.5 and 13 h for elastic and fluid transforms, respectively, on a 128×64 DECmpp1200Sx/Model 200 MASPAR (Massively Parallel Mesh-Connected Supercomputer). This spurred work to modify the algorithm to individualize atlases on standard single-processor workstations (Thirion 1995; Bro-Nielsen and Gramkow 1996; Freeborough and Fox 1998).

Bro-Nielsen and Gramkow (1996) used the eigenfunctions of the Navier–Stokes differential operator $L=\mu\nabla^2+(\lambda+\mu)\nabla(\nabla^{\mathrm{T}}\bullet)$, which governs the atlas deformations, to derive a very rapid, Green's function solution $\boldsymbol{u}^*(\boldsymbol{x})=\boldsymbol{G}(\boldsymbol{x})$ to the impulse response equation $L\boldsymbol{u}^*(\boldsymbol{x})=\delta(\boldsymbol{x}-\boldsymbol{x}_0)$. This speeds up the core registration step by a factor of 1000. The solution to the full PDE $L\boldsymbol{u}(\boldsymbol{x})=-\boldsymbol{F}(\boldsymbol{x})$ was approximated as a rapid filtering operation on the 3D arrays representing body force components:

$$\boldsymbol{u}(\boldsymbol{x})=-\int_{\Omega}\boldsymbol{G}(\boldsymbol{x}-\boldsymbol{r})\cdot\boldsymbol{F}(\boldsymbol{r})d\boldsymbol{r}=-\left(\boldsymbol{G}^*\boldsymbol{F}\right)(\boldsymbol{x})\,, \quad (16)$$

where $\boldsymbol{G}^*$ represents convolution with the impulse response filter. As noted in (Gramkow and Bro-Nielsen 1997), a recent fast, 'demons-based' warping algorithm (Thirion 1995; Dawant et al. 1998; Cachier et al. 1999) calculates the atlas flow velocity by regularizing the force field driving the template with a Gaussian filter (cf. Collins et al. 1994). Since this filter is a separable approximation to the continuum–mechanical filters derived above (Nielsen et al. 1994), interest has focused on deriving additional separable (and therefore computationally fast) filters to create subject-specific brain atlases and rapidly label new images (Gramkow 1996; Lester et al. 1999). Ultimately, filtering the driving force, as well as the deformation field (or its increments) are central to high-dimensional non-linear registration. With this in mind, Cachier et al. (1999) developed an *a posteriori* filter-weighting approach that attenuates the weight of the driving force at positions where it leads to a poorer match. Fast multigrid solvers have also accelerated systems for atlas-based segmentation and labeling (Dengler and Schmidt 1988; Bajcsy and Kovacic 1989; Collins et al. 1994, 1995; Gee et al. 1993,1995; Schormann et al. 1996). Some of these now have sufficient speed for real-time surgical guidance applications (Warfield et al. 1998).

Neural net implementations

Neural networks can also be used in an ingenious way to recover anatomic correspondences in a database. To see this, note that the simplest set of anatomic features that can guide the mapping of one brain to another is a set of point landmarks. Point correspondences can be extended to produce a deformation field for the full volume using a spline formula, which specifies how to interpolate the displacement field $\boldsymbol{u}(\boldsymbol{x})$ from a set of points $\{\boldsymbol{x}_i\}$ to the surrounding 2D plane or 3D volume:

$$\boldsymbol{u}(\boldsymbol{x})=p_{m-1}(\boldsymbol{x})+\sum_i c_i G(\boldsymbol{x}-\boldsymbol{x}_i)\,. \quad (17)$$

Here $p_{m-1}(\boldsymbol{x})$ is a polynomial of total degree $m-1$, where m is the order of derivative used in the regularizer, and G is a *radial basis function* (RBF) or Green's function whose form depends on the type of spline being used (Joshi et al. 1995; Davis et al. 1997). Choices of $r^2\ln r$ and r correspond to the *thin-plate spline* in 2D and 3D, with r^3 for the

3D *volume spline* (Davis et al. 1997), and the 3×3 matrix $\left[\alpha r^2 \boldsymbol{I} - 3\boldsymbol{x}\boldsymbol{x}^{\mathrm{T}}\right] r$ for the 3D *elastic body spline* (Davis et al. 1997). Substitution of the point correspondences into this formula results in linear system that can be solved for the deformation field (Fig. 3; Thompson and Toga 1998). Neural network approaches exploit this by using correspondences at known landmarks as a *training set* to learn a multivariate function. This function maps positions in the image (input) to the desired displacement field at that point (output). Intriguingly, the hidden units in the neural net are directly analogous to Green's functions, or convolution filters, in the continuum–mechanical matching approach (Joshi et al. 1995; Bro-Nielsen and Gramkow 1996). By converting the above linear system into a neural network architecture, the k deformation field components are the output values of the neural net:

$$\boldsymbol{u}^k(\boldsymbol{x}) = \sum_{m=1 \text{ to } M} a_m \pi_m(\boldsymbol{x}) + \sum_{i=1 \text{ to } N} w_{ik} G_i\left(\boldsymbol{x} - \boldsymbol{x}_i\right) . \qquad (18)$$

Here the G_i are N separate hidden unit neurons with receptive fields centered at $\boldsymbol{x}_i$, $\sum a_m \pi_m$ is a polynomial whose terms are hidden units and whose coefficients a_m are also learned from the training set, and w_{ik} are synaptic weights (Fig. 3). The synaptic weights are determined by solving a linear system obtained by substituting the training data into this equation. If landmarks are available to constrain the mapping, the function centers $\boldsymbol{x}_i$ may be initialized at the landmark positions, otherwise hidden units can initially be randomly placed across the image (Davis et al. 1996). Network weights (the coordinate transformation parameters) and the RBF center locations are successively tuned to optimize an intensity-based functional (normalized correlation or mutual information) that measures the quality of the match. The network is trained (i.e., the parameters of the warping field are determined) by evaluating the gradient of the normalized correlation with respect to the network parameters, and optimizing their values by gradient descent. Results matching 3D brain image pairs were impressive (Davis et al. 1996). The close relationship between continuum–mechanical PDEs, statistical regression and neural nets (see Ripley et al. 1996) has led to their independent appearance in several approaches for computational anatomy.

4 Mapping the cortex

Deformable atlases have broad applications in the automated labeling of deep anatomical structures in the brain, and in the estimation of gross neuroanatomical variability (Collins et al. 1995; Giedd et al. 1999). Nonetheless, a major barrier in their use has been the extreme variability of the anatomy of the human cerebral cortex. Deformable atlases will not in general deform to match the correct regions of cortex in new subjects, unless the algorithms are given additional information on the locations of sulci or gyri.

Understanding cortical anatomy and function is a major focus in brain research. Many diseases affect the anatomy and organization of the cortex. The cortex also changes over time, as in aging, Alzheimer's disease (Mega et al. 2000), or developmental disorders (Sowell et al. 1999; Thompson et al. 1998, 2001; Blanton et al. 2001). The gyral patterns of the human cortex provide a fairly reliable guide to its functional organization, although the congruence is not absolute (Brodmann 1909; Rademacher et al. 1993). Since most imaging studies of brain function also focus on the cortex, it is especially important to reliably pool brain mapping data from subjects whose anatomy is different (Zeineh et al. 2001). Despite interest in analyzing patterns of cortical variation for interesting effects, general patterns of organization are hard to discern, as are systematic alterations in disease. The peculiar fissure patterns in the cortex (Fig. 4) also complicate attempts to define statistical criteria for abnormal cortical anatomy.

In the following section we outline a framework for analyzing cortical anatomy. Specialized algorithms compare and average cortical anatomy across subjects and groups, map its

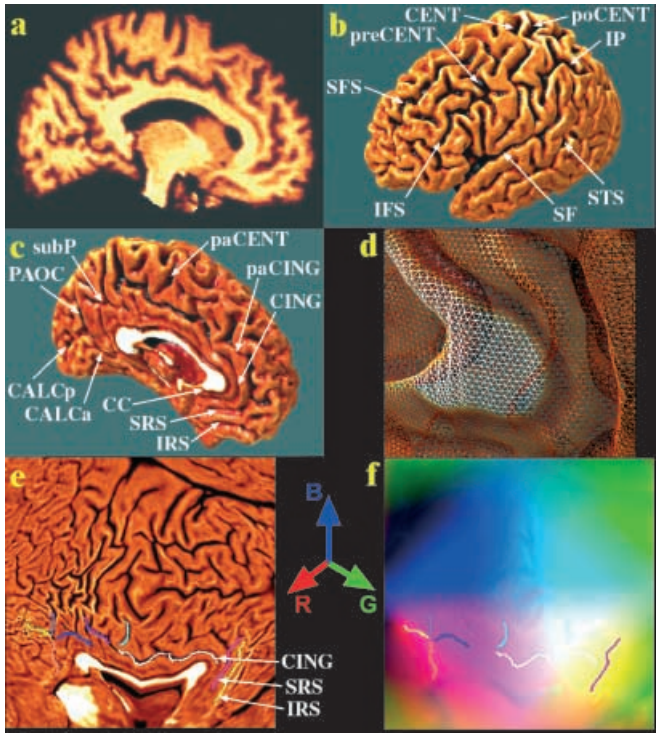

Fig. 4a–f. Measuring differences in cortical anatomy. Based on an individual's 3D MRI scan (**a**), detailed surface models of the cerebral cortex can be generated (**b**),(**c**). A template of 3D curved lines is delineated on these surfaces, capturing the morphology of the sulcal pattern. On the lateral brain surface, important functional landmarks include the central (CENT), pre- and post-central (preCENT, poCENT), superior and inferior frontal sulci (SFS, IFS), intraparietal sulcus (IP), Sylvian fissure (SF) and superior temporal sulcus (STS). Medial surface landmarks include the corpus callosum (CC), anterior and posterior calcarine (CALCa/p), parieto-occipital, subparietal, paracentral, paracingulate, and cingulate sulci, and the superior and inferior rostral sulci. A spherically-parameterized, triangulated 3D mesh represents the cortical surface; **d** shows the grid structure around the anterior corpus callosum. When the parameter space of the surface is flattened out (**e**), landmarks in the folded brain surface can be reidentified (e.g. IRS, SRS, etc.). (The white patch by the *corpus callosum* is where the surface model cuts across the white matter of the brain stem). To avoid loss of 3D information in the flattening, a color code is used to store where each flat map location came from in 3D, with red colors brighter where the lateral (X) coordinate is larger, green colors brighter where the posterior-to-anterior coordinate (Y) is larger, etc. The warping of these color maps (Fig. 5), and the averaging of the resulting images, provides a surprising strategy for creating average cortical models for a group of subjects, and for exploring cortical pattern variation

variation and asymmetry, and chart patterns of abnormality or brain change. These approaches draw heavily on the deformable atlas approaches described already, but supplement them with additional modeling approaches that make comparison of cortical data tractable.

Cortical modeling

A major challenge in investigations of disease is to determine (1) whether cortical organization is altered, and if so, which cortical systems are implicated, and (2) whether normal features of cortical organization are lost, such as sulcal pattern asymmetries (Kikinis et al. 1994; Narr et al. 2001; Sowell et al. 2001). This requires methods to create a well-resolved average model of the cortex specific for a diseased group, and a statistical framework to compare individual and group average models with normative data.

Several methods exist to generate surface models of the cortex from 3D MRI scans. Some of these impose a tiled, parametric grid structure on the anatomy as a coordinate framework for subsequent computations. In 'bottom-up' approaches, a voxel-based segmentation of white matter is generated, using a tissue classifier or level set methods (Sapiro 2000), and is tiled using marching cubes. The resulting triangulation is corrected, using graph theoretic methods, or computation of its Euler characteristic, to create a single, simply connected, closed surface homeomorphic to a sphere (Fischl et al. 1999; Hurdal et al. 2000; Rettman et al. 2000; Shattuck et al. 2001). The resulting gridded surface can then be inflated, using iterative smoothing, to a spherical shape. This allows a spherical coordinate system to be projected back onto the 3D model, for subsequent computations. Alternatively the 3D surface may be flattened to a 2D plane (Fig. 4; Drury and Van Essen et al. 1997; Thompson et al. 1997; Angenent et al. 1999; Hurdal et al. 2000), inducing an alternative 2D parameterization onto the original 3D surface.

In 'top-down' surface extraction approaches (Davatzikos 1996; MacDonald 1998), a spherical parametric surface is created at the outset. The positions of the nodes are successively moved, under image-dependent forces, reshaping it into the complex geometry of the cortical boundary. This avoids the need for topology correction, as a single, fixed, grid structure is established at the start, and mapped with a continuous deformation onto each anatomy. Complex constraints are, however, required while deforming the surface, to ensure the surface does not self-intersect and adapts fully to the target geometry (see Xu et al. 1999, for work on *gradient vector flow*).

Mapping gyral pattern differences

Once cortical models are available for a large number of subjects, in a common 3D coordinate space, patterns of cortical variability can be encoded. The major gyri (ridges) and sulci (fissures) of the cortical surface have a similar spatial organization across subjects (Regis 1994), even though their geometry varies substantially. Recently, we specified a maximal set, or template, containing all primary sulci that consistently occur in normal subjects[2] (see Footnote 2; Fig. 4b,c shows some of these). This set of sulcal curves can be very reliably identified by trained raters, so long as a formalized protocol and detailed anatomical criteria are followed (Sowell et al. 2001). We currently use a manual approach as automated labeling of sulci is extremely difficult, and is the focus of intense study by our group and others (Mangin et al. 1994; MacDonald 1998; Lohmann et al. 1999; Vaillant et al. 1999; Le Goualher et al. 1999; Zhou et al. 1999; Rettman et al. 2000; Tao et al. 2001).

Mapping cortical patterns

Cortical anatomy can be compared, between any pair of subjects, by computing the warped mapping that elastically transforms one cortex into the shape of the other. Due to variations in gyral patterning, cortical differences among subjects will be severely underestimated unless elements of the gyral pattern are matched from one subject to another. This matching is also required for cortical averaging; otherwise, corresponding gyral features will not be averaged together. Transformations can therefore be developed that match large networks of gyral and sulcal features with their counterparts in the target brain (Thompson and Toga 1996, 1997; Davatzikos 1996; Van Essen et al. 1997; Fischl et al. 1999). In our approach, we match 38 elements of the gyral pattern, including the major features that are consistent in their incidence and topology across subjects (see Thompson et al. 2001 for details; Sowell et al. 2000; cf. Ono et al. 1990; Leonard et al. 1996; Kennedy et al. 1998).

To find good matches among cortical regions we perform the matching process in the cortical surface's parametric space, which permits more tractable mathematics (Fig. 5). This vector flow field in the parametric space indirectly specifies a correspondence field in 3D, which drives one cortical surface into the shape of another. This mapping not only matches overall cortical geometry, but matches the entire network of the 38 landmark curves with their counterparts in the target brain, and thus is a valid encoding of cortical variation.

Spherical, planar maps of cortex

We recently applied this matching approach to measure anatomic variability in a database of 96 cortical models (extracted from an MRI database with the algorithm of MacDonald 1998). Since cortical models were created by driving a tiled, spherical mesh into the configuration of each

[2] Several complications arise in identifying corresponding sulci across subjects, but these can usually be resolved using information on which sulci border known architectonic fields (Brodmann 1909; Rademacher et al. 1993). Approximately a quarter of normal brain hemispheres have two cingulate gyri (the 'double parallel' conformation; Ono et al. 1990; Regis 1994; Paus et al. 1999), and some individuals have two Heschl's gyri (Leonard et al. 1996), while others have only one. When there are two cingulate sulci, the outer (paracingulate) sulcus arguably matches the single sulcus in an individual with only one, as it bounds the Brodmann areas belonging to the limbic system. Interrupted sulci, in which a sulcal curve is broken into several segments, may also need to be connected and modeled as a single curve to facilitate matching (cf. Thompson et al. 1999; Sebastian et al. 2000). In rare cases, some pairs of sulci, such as the postcentral sulcus and the marginal ramus of the cingulate, meet the superior margin of the interhemispheric fissure in a different anterior-to-posterior order. Modeling of the graph-theoretic structure and connectivity of the sulci may also be necessary for a fuller understanding of cortical variation (Mangin et al. 1994).

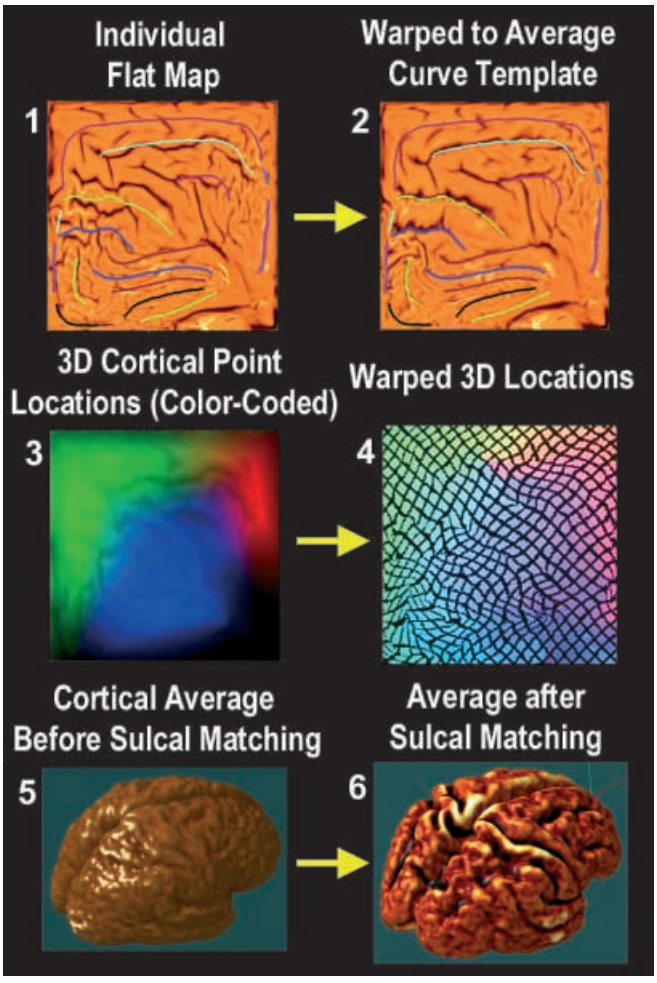

Fig. 5. Cortical pattern matching and averaging. A well-resolved average cortical model (*panel 6*) for a group of subjects can be created by first flattening each subject's cortical model to a 2D square (*panel 1*; see also Fig. 4). A color coded map (3) stores a unique color triplet (RGB) at each location in the 2D parameter space encoding the (x, y, z) coordinate of the 3D cortical point mapped to that 2D location. By averaging these color maps pixel-by-pixel across subjects, and then decoding the 3D colors into a surface model, a smooth cortical model (5) is produced. However, a well-resolved average model (6) is produced, with cortical features in their group mean location, if each subject's color map is first flowed (4) so that sulcal features are driven into the configuration of a 2D average sulcal template (2). The average curve set is defined by 2D vector averaging of many subjects' flattened curves. In this flow (4), codes indexing similar 3D anatomical features are placed at corresponding locations in the parameter space, and are thus reinforced in the group average (6)

subject's cortex, any point on the cortical surface maps to exactly one point on the sphere and *vice versa*. Each cortical surface is parameterized with an invertible mapping $D_p, D_q : (r, s) \rightarrow (x, y, z)$, so sulcal curves and landmarks in the folded brain surface can be reidentified in a spherical map (cf. Fischl et al. 1999). To retain relevant 3D information, cortical surface point position vectors (x, y, z) in 3D stereotaxic space were color-coded using a unique RGB color triplet, to form an image of the parameter space in color image format (Fig. 4f). These spherical locations, indexed by two parameters, can also be mapped to a plane (Fig. 4e; Thompson et al. 1997). Cortical differences between any pair of subjects were calculated as follows. A flow field was first calculated that elastically warps one flat map onto another from the other subject (Fig. 5; or equivalently, one spherical map onto the other). On the sphere, the parameter shift function $\boldsymbol{u}(\boldsymbol{r}) : \Omega \rightarrow \Omega$, is given by the solution $F_{pq} : \boldsymbol{r} \rightarrow \boldsymbol{r} - \boldsymbol{u}(\boldsymbol{r})$ to a curve-driven warp in the spherical parametric space $\Omega = [0, 2\pi) \times [0, \pi)$ of the cortex (Fig. 5; Thompson et al. 1997). For points $\boldsymbol{r} = (r, s)$ in the parameter space, a system of simultaneous partial differential equations can be written for the flow field $\boldsymbol{u}(\boldsymbol{r})$:

$$L^{\ddagger}\left(\boldsymbol{u}(\boldsymbol{r})\right) + \boldsymbol{F}\left(\boldsymbol{r} - \boldsymbol{u}(\boldsymbol{r})\right) = \boldsymbol{0}\,, \quad \forall \boldsymbol{r} \in \Omega\,,$$
$$\text{with} \quad \boldsymbol{u}(\boldsymbol{r}) = \boldsymbol{u}_0(\boldsymbol{r})\,,\ \forall \boldsymbol{r} \in M_0 \cup M_1\,. \tag{19}$$

Here M_0, M_1 are sets of points and (sulcal or gyral) curves where displacement vectors $\boldsymbol{u}(\boldsymbol{r}) = \boldsymbol{u}_0(\boldsymbol{r})$ matching corresponding anatomy across subjects are known. The flow behavior is modeled using equations derived from continuum mechanics, and these equations are governed by the Cauchy–Navier differential operator $L = \mu\nabla^2 + (\lambda + \mu)\nabla(\nabla^{\mathrm{T}}\bullet)$ with body force $\boldsymbol{F}$ (Bajcsy and Kovacic 1989; Gramkow 1998). The only difference is that $L^{\ddagger}$ is the *covariant* form of the differential operator L (for reasons explained in footnote 3)[3].

[3] *Covariant mapping equations.* Since the cortex is not a *developable* surface, it cannot be given a parameterization whose metric tensor is uniform. As in fluid dynamics or general relativity applications, the intrinsic curvature of the solution domain can be taken into account when computing flow vector fields in the cortical parameter space, and mapping one mesh surface onto another. In the *covariant tensor* approach (Thompson et al. 2001), correction terms (Christoffel symbols, $\boldsymbol{\Gamma}^i_{jk}$) make the necessary adjustments for fluctuations in the metric tensor of the mapping procedure. In the partial differential equations (1), we replace L by the covariant differential operator $L^{\ddagger}$. In $L^{\ddagger}$, all L's partial derivatives are replaced with *covariant* derivatives (Burke 1985). These covariant derivatives are defined with respect to the metric tensor of the surface domain where calculations are performed. The covariant derivative of a (contravariant) vector field, $u^i(\boldsymbol{x})$, is defined as $u^i_{,k} = \partial u^j/\partial x^k + \boldsymbol{\Gamma}^i_{jk} u^i$ where the *Christoffel symbols of the second kind* (Einstein 1914), $\boldsymbol{\Gamma}^i_{jk}$, are computed from derivatives of the metric tensor components $g_{jk}(\boldsymbol{x})$:

$$\boldsymbol{\Gamma}^i_{jk} = (1/2) g^{il}\left(\partial g_{lj}/\partial x^k + \partial g_{lk}/\partial x^j - \partial g_{jk}/\partial x^i\right)\,. \tag{20}$$

These correction terms are then used in the solution of the Dirichlet problem (Joshi et al. 1995) to match one cortex with another. Note that a parameterization-invariant variational formulation could also be used to minimize metric distortion when mapping one surface to another. If P and Q are cortical surfaces with metric tensors $g_{jk}(u^i)$ and $h_{jk}(\xi^\alpha)$ in local coordinates u^i and $\xi^\alpha (i, \alpha = 1, 2)$, the *Dirichlet energy* of the mapping $\xi(u)$ is defined as: $E(\xi) = \int_{\boldsymbol{P}} \mathrm{e}(\xi)(u) dP$, where $\mathrm{e}(\xi)(u) = g^{ij}(u)\partial\xi^\alpha(u)/\partial u^i \partial\xi^\beta(u)/\partial u^j h_{\alpha\beta}(\xi(u))$ and $dP = \left(\sqrt{\det\left[g_{ij}\right]}\right) du^1 du^2$. The Euler equations, whose solution $\xi^\alpha(u)$ minimizes the mapping energy, are:

$$0 = L\left(\xi^i\right) = \sum_{m=1\,\text{to}\,2} \partial/\partial u^m \times \left[\left(\sqrt{\det\left[g^{ru}\right]}\right) \sum_{l=1\,\text{to}\,2} g^{ml}_{ur} \partial\xi^i \big/ \partial u^l\right] \quad (i = 1, 2)\,, \tag{21}$$

(Liseikin 1991). The resulting (harmonic) map (1) minimizes the change in metric from one surface to the other, and (2) is again independent of the parameterizations (spherical or planar) used for each surface. The harmonic energy is therefore a functional defined on a quotient space, being invariant to the action of the reparameterization group on each surface [see Srivastava et al. 1999 for similar group-invariant metrics; related algorithms for minimizing harmonic energies, invariant under re-parameterization, have been developed in level set methods for image restoration (Bertalmio et al. 2000), signal detection and smoothing on surfaces (Chung et al. 2000), in modeling liquid crystals (Alouges 1997) and in Polyakov's formulation of string theory (Polyakov 1987)].

This approach not only guarantees precise matching of cortical landmarks across subjects, but creates mappings that are independent of the surface metrics, and therefore independent of the surface parameterizations.

Cortical averaging using pull-backs and flows in parameter space

The intersubject variability of the cortex is computed by first creating an average cortex for each subject group and measuring individual differences from the deformation mappings that drive the average model onto each individual. By defining probability distributions on the space of deformation transformations applied to the average template (see Sect. 2), statistical parameters of these distributions are estimated from the databased anatomic data to determine the magnitude and directional biases of anatomic variation. To do this, all 38 gyral curves for all subjects are first transferred to the parameter space (Fig. 4e). Next, each curve is uniformly re-parameterized to produce a regular curve of 100 points whose corresponding 3D locations are uniformly spaced. A set of 38 average gyral curves for the group is created by vector averaging all point locations on each curve. This *average curve template* (*curves* in Fig. 5a) serves as the target for alignment of individual cortical patterns (Thompson et al. 2000; Zeineh et al. 2001). Each individual cortical pattern is transformed into the average curve configuration using a flow field in the parameter space (Fig. 5b; cf. Bakircioglu et al. 1999). By carrying a color code (that indexes 3D locations; Fig. 5c) along with the vector flow that aligns each individual with the average folding pattern, information can be recovered at a particular location in the average folding pattern (Fig. 5d) specifying the 3D cortical points mapping each subject to the average. In the language of Lie algebras, corresponding 3D cortical points across the subject database are defined as the *pull-back* $D_p^*(\boldsymbol{r})$ (Burke 1985) of the parameterization mappings $D_p : (r, s) \rightarrow (x, y, z)$ under the covariant vector flow $\boldsymbol{u}(\boldsymbol{r})$ that maps each subject to the average curve template. [For any smooth function $D_p : \Omega \rightarrow R^n$ and any diffeomorphic map $\boldsymbol{u}(\boldsymbol{r}) : \Omega \rightarrow N$, there is a function on N, $D_p^* : N \rightarrow R^n$ called the pull-back of D_p by $\boldsymbol{u}(\boldsymbol{r})$, and defined by $D_p \circ \boldsymbol{u}$ (Burke 1987)].

This produces a new coordinate grid [the *pull-back* $D_p^*(\boldsymbol{r})$; Fig. 5d] on a given subject's cortex in which particular gridpoints appear in the same location across subjects relative to the mean gyral pattern. By averaging these 3D positions across subjects, an average 3D cortical model can be constructed for the group. An example of this type of cortical average, based on 9 subjects with Alzheimer's disease, is shown in Fig. 5f. The resulting mapping is guaranteed to average together all points falling on the same cortical locations across the set of brains, and ensures that corresponding features are averaged together.

Average brain templates

Maps that deform individual cortical patterns into a group average shape can also assist in generating a brain template with the mean shape for a group, and with sharply defined geometry. We recently used high-dimensional transformations to create a mean image template for a group of patients with Alzheimer's disease (AD), whose anatomy is not well accommodated by existing brain atlases or imaging templates (Thompson et al. 2001). We introduce this idea now, as in later sections we will typically use an average brain coordinate space as the space in which anatomical variability is quantified.

To make a mean image template for a group, several approaches are possible (Evans et al. 1994; Subsol 1995; Grenander and Miller 1998; Guimond et al. 1999; Thompson et al. 2000; Woods et al. 2000). If scans are mutually aligned using only a linear transformation (Fig. 6), the resulting average brain is blurred in the more variable anatomic regions, and cortical features are washed away. The resulting average brain also tends to exceed the average dimensions of the component brain images. By averaging geometric and intensity features separately (cf. Ge et al. 1995; Bookstein 1997; Grenander and Miller 1998; Christensen et al. 1999; Thompson et al. 2000), a template can be made with the mean intensity and geometry for a patient population. To illustrate this, we generated an initial image template for a group of Alzheimer's patients by (1) using automated linear transformations (Woods et al. 1993) to align the MRI data with a randomly selected image, (2) intensity-averaging the aligned scans, and then (3) recursively re-registering the scans to the resulting average affine image. The resulting average image was adjusted to have the mean affine shape for the group using matrix exponentiation to define average transformations (Woods et al. 1998). Images and a large set of anatomical surface models (84 per subject) were then linearly aligned to this template, and an average surface set was created for the group. Displacement maps driving the surface anatomy of each subject into correspondence with the average surface set were then computed, and were extended to the full volume with surface-based elastic warping (Thompson et al. 2000; see also Fig. 2). These warping fields reconfigured each subject's 3D image into the average anatomic configuration for the group. By averaging the reconfigured images (after intensity normalization), a crisp image template was created to represent the group (Fig. 6). Note the better-resolved cortical features and sharper definition of tissue boundaries in the average images after high-dimensional cortical registration. If desired, this AD-specific atlas can retain the coordinate matrix of the Talairach system (with the anterior commissure at $(0, 0, 0)$) while refining the gyral map of the Talairach atlas to encode the unique anatomy of the AD population. By explicitly computing matching fields that relate gyral patterns across subjects, a well-resolved and spatially consistent set of probabilistic anatomical models and average images can be made to represent the average anatomy and its variation in a subpopulation.

Uses of average templates

Average brain templates have a variety of uses. If functional imaging data from Alzheimer's patients is warped into an atlas template based on young normals, signals in regions with selective atrophy in disease are artificially expanded to match their scale in young normals, and biases can result. If the atlas

has the average geometry for the diseased group, which may include atrophy, least distortion is applied by warping data into the atlas. Since the template (in Fig. 6) also has the average affine shape for the group (Woods et al. 1998), least distortion is applied when either linear, non-linear, approaches are used. The notion of least distortion can be formulated precisely using either (1) mean vector fields (Thompson et al. 2000; Kochunov et al. 2001); (2) the associated matrix and deformation tensor metrics (Woods et al. 2000), or (3) using the L^2-norm on the Hilbert space of deformation field coefficients (Grenander and Miller 1998; cf. Martin et al. 1994), or (4) indirectly through a continuum-mechanical operator or regularization functional that defines what it means for a distortion to be irregular (Christensen et al. 1999; Miller and Younes 2001).

For a given nonlinear registration algorithm, and after affine components of deformation are factored out, a 'mean-field average brain template' is one for which:

$$\sum_{i=1 \text{ to } N} \int_{\Omega} \|\boldsymbol{u}_i(\boldsymbol{x})\|^p \, d\boldsymbol{x} \,, \tag{22}$$

is minimal, when $\boldsymbol{u}_i(\boldsymbol{x})$ are the deformations mapping it onto a large set of other brains ($p = 1$ or 2 correspond to different norms). Alternatively, a 'mean-energy average brain template' is one for which:

$$\sum_{i=1 \text{ to } N} \int_{\Omega} \left\| \boldsymbol{L}^{\ddagger} \boldsymbol{u}_i(\boldsymbol{x}) \right\|^p d\boldsymbol{x} \,, \tag{23}$$

is minimal. Here $\boldsymbol{L}$ is a (possibly covariant; see above) differential operator defining the energetics of the deformation field, ‡ denotes covariant differentiation with respect to the metric of the base manifold (this has no effect unless we are averaging non-flat manifolds, such as cortical surfaces, where the Christoffel symbols do not vanish). Extending these ideas to registration algorithms that use velocity fields to ensure diffeomorphic mappings (e.g., Christensen et al. 1996; see above), Miller and Younes (2001) show that:

$$\arg\min \boldsymbol{\nu} \in V \int_{\Omega \times [0,1]} \|\boldsymbol{L}\boldsymbol{v}(\boldsymbol{x}, t)\|^2 \, d\boldsymbol{x} \, dt \,, \tag{24}$$

defines a metric on the space of diffeomorphisms, where V is the space of all velocity fields (paths) that deform the reference anatomy at $t = 0$ onto a target anatomy at time $t = 1$. In their formulation, a mean brain template would be one for which the following average energy is minimized:

$$\sum_{i=1 \text{ to } N} \int_{\Omega} \|\boldsymbol{L}\,(\boldsymbol{v}_i(\boldsymbol{x}, t))\|^2 \, d\boldsymbol{x} \,. \tag{25}$$

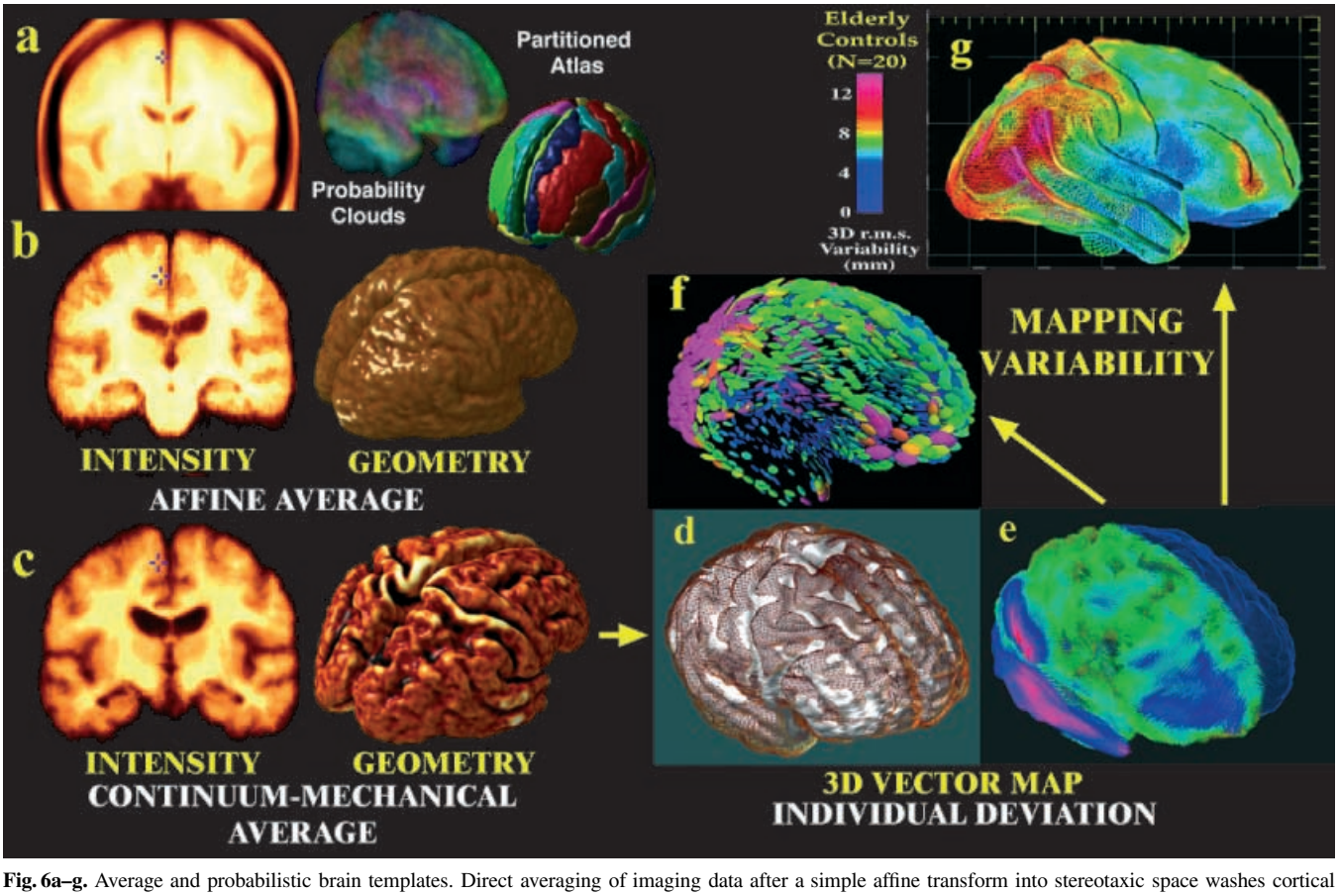

Fig. 6a–g. Average and probabilistic brain templates. Direct averaging of imaging data after a simple affine transform into stereotaxic space washes cortical features away ((**a**); Evans et al. 1994; $N = 305$ normals; **b** shows a similar approach with $N = 9$ Alzheimer's patients). By first averaging a set of vector-based 3D geometric models, and warping each subject's scan into the average configuration (as in Fig. 5), a well-resolved average brain template is produced (**c**). Deformation vector maps **d** store individual deviations (*brown mesh*) from a group average (white surface, (**e**)), and their covariance fields **f** store information on the preferred directions and magnitude (**g**) of anatomic variability (*pink colors, large variation; blue colors, less*)

As a result, average brain image templates can be derived in various different ways. The one in Fig. 6 has the mean geometry *and mean intensity* for a group. In Kochunov et al. (2001), we used an extremely high-resolution brain image (an average of 27 MRI scans of the same subject (Holmes et al. 1998)) and optimized its geometry. The individuality of brain shape was removed by deforming the high-resolution template to 30 brains, and applying the mean deformation field to the template. Interestingly, automated registration approaches were able to reduce anatomic variability to a statistically greater degree if this specially-prepared image template was used as a registration target (Kochunov et al. 2001). With smaller deformations, non-global minima of the registration measure may be avoided, and convergence may also be faster, as the parameter space is searched for an optimal match. This optimality of average brain templates may be advantageous when databases are mined for information using nonlinear registration as an information source.

Average templates are under rapid development for the *Macaque* brain (Grenander and Miller 1998), and for individual structures such as the *corpus callosum*, (Davatzikos 1996; Gee et al. 1998), central sulcus (Manceaux-Demiau et al. 1998), cingulate and paracingulate sulci (Paus et al. 1996; Thompson et al. 1997), hippocampus (Haller et al. 1997; Joshi et al. 1998; Csernansky et al. 1998; Thompson et al. 1999) and for transformed representations of the human and *Macaque* cortex (Van Essen et al. 1997; Grenander and Miller 1998; Thompson et al. 1999; Fischl et al. 1999).

Mapping anatomic variability

Once anatomic data are aligned with an average brain template, maps of anatomic variability can be generated and used a reference to assess abnormalities in an individual or group. By using cortical pattern matching to identify corresponding cortical locations in 3D space, rather than simple image averaging (Fig. 6a,b), deformation maps can be recovered mapping each patient into gyrus-by-gyrus correspondence with the average cortex (Fig. 6e). Anatomic variability can thus be defined at each point on the average cortical mesh as the root mean square magnitude of the 3D displacement vectors, assigned to each point, in the surface maps from individual to average. This variability pattern is visualized as a color-coded map (Fig. 6g). This map shows the anatomic differences, due to gyral pattern variation, that remain after affine alignment of MR data into a brain template with the mean shape and intensity for the group.

After these affine components of the deformation fields are factored out, the deformation vector required to match the structure at position $\boldsymbol{x}$ in the average cortex with its counterpart in subject i can be modeled as:

$$\boldsymbol{W}_i(\boldsymbol{x}) = \boldsymbol{\mu}(\boldsymbol{x}) + \boldsymbol{\Sigma}(\boldsymbol{x})^{1/2}\boldsymbol{\epsilon}_i(\boldsymbol{x})\,. \tag{26}$$

Here $\boldsymbol{\mu}(\boldsymbol{x})$ is the mean deformation vector for the population (which approaches the zero vector for large N), $\boldsymbol{\Sigma}(\boldsymbol{x})$ is a non-stationary, anisotropic covariance tensor field estimated from the mappings, $\boldsymbol{\Sigma}(\boldsymbol{x})^{1/2}$ is the upper triangular Cholesky factor tensor field, and $\epsilon_i(\boldsymbol{x})$ can be modeled as a trivariate random vector field whose components are inde pendent zero-mean, unit variance, stationary random fields. This 3D probability distribution makes it possible to visualize the principal directions (eigenvectors) as well as the magnitude of gyral pattern variability, and these characteristics are highly heterogeneous across the cortex. For any desired confidence threshold α, $100(1-\alpha)$ *confidence regions* for possible locations of points corresponding to $\boldsymbol{x}$ on the average cortex are given by nested ellipsoids $\boldsymbol{E}_{\lambda(\alpha)}(\boldsymbol{x})$ in displacement space (Fig. 2f). Here $\boldsymbol{E}_{\lambda}(\boldsymbol{x}) = \left\{\boldsymbol{\mu}(\boldsymbol{x}) + \lambda\,[\boldsymbol{\Sigma}(\boldsymbol{x})]^{-1/2}\,\boldsymbol{p} \mid \forall \boldsymbol{p} \in \boldsymbol{B}(\boldsymbol{0};1)\right\}$, where $\boldsymbol{B}(\boldsymbol{0};1)$ is the unit ball in $\mathbb{R}^3$, and $\lambda(\alpha) = \left[N(N-3)/3(N^2-1)\right]^{-1} F_{\alpha,3,N-3}$, where $F_{\alpha,3,N-3}$ is the critical value of the F distribution such that $Pr\{F_{3,N-3} < F_{\alpha,3,N-3}\} = \alpha$ and N is the number of subjects.

Detecting group anatomic differences with random fields

An analogous approach can be used to detect group differences in brain structure. Specifically, the significance of a difference in brain structure between two subject groups (e.g., patients and controls) of N_1 and N_2 subjects is assessed by calculating the sample mean and variance of the deformation fields ($j = 1, 2$):

$$\begin{aligned}
&\boldsymbol{W}_j^{\mu}(\boldsymbol{x}) = \sum_{i=1\text{ to }N_j} \boldsymbol{W}_{ij}(\boldsymbol{x})/N_j \\
&\boldsymbol{\Psi}(\boldsymbol{x}) = (1/\,[N_1 + N_2 - 2]) \\
&\times \left\{ \sum_{j=1\text{ to }2} \sum_{i=1\text{ to }N_j} \left[\boldsymbol{W}_{ij}(\boldsymbol{x}) - \boldsymbol{W}_j^{\mu}(\boldsymbol{x})\right]\left[\boldsymbol{W}_{ij}(\boldsymbol{x}) - \boldsymbol{W}_j^{\mu}(\boldsymbol{x})\right]^{\mathrm{T}} \right\}.
\end{aligned} \tag{27}$$

and computing the following statistical map (Thompson et al. 1997; Cao and Worsley 2001):

$$\begin{aligned}
T^2(\boldsymbol{x}) = {} & \{N_1 N_2/\,(N_1 + N_2)\,(N_1 + N_2 - 2)\} \\
& \times \left[\boldsymbol{W}_2^{\mu}(\boldsymbol{x}) - \boldsymbol{W}_1^{\mu}(\boldsymbol{x})\right]^{\mathrm{T}} [\boldsymbol{\Psi}(\boldsymbol{x})]^{-1} \\
& \times \left[\boldsymbol{W}_2^{\mu}(\boldsymbol{x}) - \boldsymbol{W}_1^{\mu}(\boldsymbol{x})\right].
\end{aligned} \tag{28}$$

Under the null hypothesis, $(N_1 + N_2 - 2)T^2(\boldsymbol{x})$ is a stationary Hotelling's T^2-distributed random field. At each point, if we let $\nu = (N_1 + N_2 - 2)$ and we let the dimension of the search space be $d = 3$, then:

$$F(\boldsymbol{x}) = ((\nu - d + 1)/d)\,T^2(\boldsymbol{x}) \sim F_{d,(\nu-d+1)}\,. \tag{29}$$

In other words, the field can be transformed point-wise to a Fisher–Snedecor F distribution (Thompson et al. 1997). To obtain a p-value for the effect that is adjusted for the multiple comparisons involved in assessing a whole field of statistics, Cao and Worsley (2001) examined the distribution of the global maximum $T^2_{\max}$ of the resulting T^2-distributed random field under the null hypothesis. Alternatively a significance value for the whole experiment can be assigned by estimating their fraction of the statistical map that exceeds any threshold by permutation (Sowell et al. 1999a,b). This non-parametric approach avoids assumptions about the spatial autocorrelation of the process, and has been successful in functional imaging as well (Holmes et al. 1996). Subjects are randomly assigned to groups and the distribution of accidental clusters

is tabulated empirically. We have recently used this approach to detect developmental changes in brain asymmetry and gray matter distribution, as well as gray matter loss in Alzhemer's disease and schizophrenia (see Sect. 5).

Mean asymmetry

By analysis of variance in 3D deformation fields that match different subjects' anatomies, it is also possible to differentiate intra-subject (between hemisphere), inter-subject, and inter-group contributions to brain variation in human populations, and detect significant differences using null distributions for features in Hotelling's T^2 random fields. Mapping the pattern of brain asymmetry in a group is an interesting application, as asymmetry has been linked with functional lateralization (Strauss et al. 1983), handedness (Witelson 1989), language function (Davidson and Hugdahl 1994), and is thought to be diminished in some diseases (cf. Kikinis et al. 1994, Narr et al. 2001). Although the set of mappings computed so far specifies the set of cortical points that correspond across subjects, the mean asymmetry cannot yet be computed without an additional set of mappings to define the points that correspond across hemispheres. To do this, all left hemisphere sulcal curves are projected into the cortical parameter space, reflected in the vertical axis, and averaged with their flattened counterparts in the right hemisphere, to produce a second *average curve template*. Color maps (as in Fig. 5c) representing point locations in the left and right hemispheres are then subjected to a second covariant flow

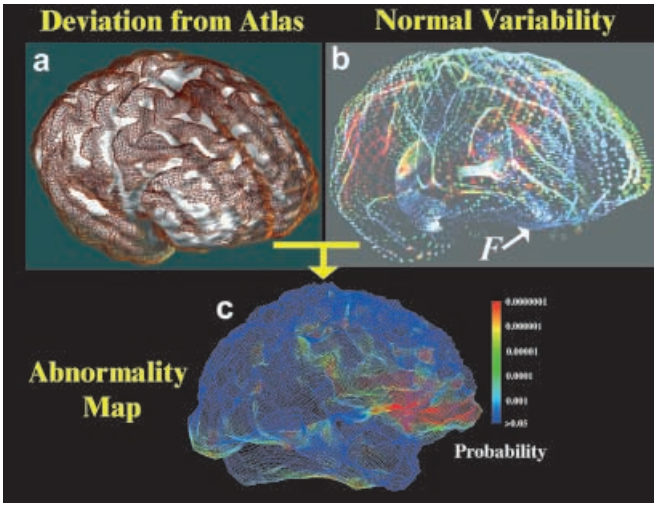

Fig. 7a–c. Abnormality detection using random fields to model anatomic variation. 3D deformation fields relating individual cortical patterns to the mean anatomical model, or atlas, (**a**), also store detailed information on how specific individuals (e.g. *brown mesh*, (**a**)) deviate from the atlas. Here residual deviations are encoded after linearly transforming a new subject's anatomy to match an average model of the cortex (*white mesh*). By computing the covariance matrix of the deformation field components, confidence limits on normal variation (**b**) can be computed. If individual deviations **(a)** are calibrated against the probability distributions that capture normal variation, abnormality maps (**c**) may be generated indicating the probability of finding the anatomy in its observed configuration in a normal population. Here, in a patient with mild Alzheimer's disease, atrophic changes are easiest to detect in orbitofrontal regions where normal variation is least (*labeled F in* **b**; *red colors* in **c**; see Thompson et al. 1996, 1997 for details)

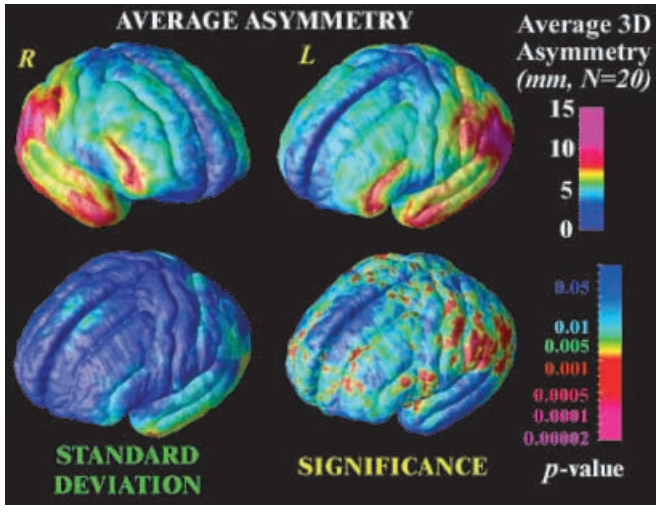

Fig. 8. Mapping brain asymmetry in a population. The average magnitude of brain asymmetry in a group ($N = 20$, *elderly normals*) can be assessed based on warping fields that map the cortical pattern of one hemisphere onto a reflected version of the other, and then flow the observations again so that corresponding measures can be averaged across subjects. Variations in asymmetry are also non-stationary across the cortex (*lower left*), and a Hotelling's T^2 statistical field can be computed to map the significance of the asymmetry (*lower right*) relative to normal anatomic variations (see text for mathematical details)

that transforms corresponding features in each hemisphere to the same location in parameter space. 3D deformation fields can then be recovered matching each brain hemisphere with a reflected version of the opposite hemisphere (cf. Thirion et al. 2000). The parameter flows are advantageous in that the asymmetry fields are also *registered*; in other words asymmetry measures can be averaged across corresponding anatomy at the cortex. This is not necessarily the case if warping fields are averaged at the same coordinate locations in stereotaxic space (cf. Fig. 6a). The pattern of mean brain asymmetry for a group of 20 subjects is shown in Fig. 8. The resulting asymmetry fields $\boldsymbol{a}_i(\boldsymbol{r})$ (at parameter space location $\boldsymbol{r}$ in subject i) were treated as observations from a spatially-parameterized random vector field, with mean $\boldsymbol{\mu}_a(\boldsymbol{r})$ and a non-stationary covariance tensor $\boldsymbol{\Sigma}_a(\boldsymbol{r})$ (Fig. 8c). The significance α of deviations from symmetry can be assessed using a T^2 or F statistic that indicates evidence of significant asymmetry in cortical patterns between hemispheres:

$$\alpha(\boldsymbol{r}) = F^{-1}_{3,N-3}\left([(N-3)/3(N-1)]\,T^2(\boldsymbol{r})\right)$$
$$\text{where } T^2(\boldsymbol{r}) = N\left[\boldsymbol{\mu}_a(\boldsymbol{r})^{\mathrm{T}}\boldsymbol{\Sigma}_a^{-1}(\boldsymbol{r})\boldsymbol{\mu}_a(\boldsymbol{r})\right]. \quad (30)$$

Using this asymmetry mapping technique, we recently observed that brain asymmetry appears to increase during childhood and adolescence (Sowell et al. 2001), and that there may also be significant asymmetries in the degree to which genes affect brain structure (Thompson et al. 2001).

5 Applications in development and disease

Gray matter loss in a diseased population

The mapping approaches introduced so far have been applied to study brain structure in Alzheimer's disease (Thompson

et al. 2000a,b; Mega et al. 1999), chronic, first-episode, and childhood-onset schizophrenia (Narr et al. 2000, 2001a,b,c), fetal alcohol syndrome (Sowell et al. 2001), as well as elucidate the pattern of brain change in childhood and adolescence (Thompson et al. 2000, 2001; Sowell et al. 2001a,b; Blanton et al. 2001).

An interesting application is in visualizing the average profile of gray matter loss across the cortex in Alzheimer's disease, based on a large number of subjects at a specific stage in the disease. Gyral pattern variation makes it difficult to make inferences if gray matter maps are directly averaged together in stereotaxic space (e.g., Fig. 6a), and the ability to localize results to specific cortical regions is also lost. To address this, we used covariant flows to assist in computing group averages and statistics. First, we segmented all images in the database with a previously validated Gaussian mixture classifier. Maps of gray matter, white matter, cerebro-spinal fluid and a background class were created for each subject (Fig. 9). The proportion of gray matter lying within 15 mm of each cortical point was then plotted as an attribute on each cortex, and aligned across subjects by projecting it into flat space (Fig. 5c) and warping the resulting attribute field with the elastic matching technique (as in Fig. 5d). (Again, the gray matter proportion can be thought of as a scalar attribute $G(\boldsymbol{r})$ defined in the cortical parameter space, which can be subjected to a *pull-back* with the flow field $\boldsymbol{u}(\boldsymbol{r})$ to compensate for gyral pattern differences). By averaging the aligned maps, and texturing them back onto a group average model of the cortex, the average magnitude of gray matter loss was computed for the Alzheimer's disease population (Fig. 9). Regions with up to 30% reduction in the measure were sharply demarcated from adjacent regions with little or no loss. The group effect size was measured by attaching a field of t statistics, $t(\boldsymbol{r})$, to the cortical parameter space, and computing the area of the t field on the group average cortex above a fixed threshold ($p < 0.01$, uncorrected). In a multiple comparisons correction, the significance of the overall effect was confirmed to be $p < 0.01$, by permuting the assignment of subjects to groups 1 000 000 times. (The resulting $46 \times 65\,536 \times 10^6 \cong 3.0 \times 10^{12}$ linear regressions – for 46 subjects, 65 536 cortical points, and 10^6 permutations – were run in parallel on an SGI *RealityMonster* with 32 R10000 180 MHz internal CPUs, requiring 33 CPU hours in total).

Dynamic brain change

In a second application, the same procedure was applied to longitudinal MRI data from 12 schizophrenic patients and 12 adolescent controls scanned at both the beginning and end of a 5-year interval. The goal was to estimate the average rate of gray matter loss at the cortex, by matching cortical patterns and comparing changes in disease with normal changes in controls. Cortical models and gray matter measures were elastically matched first within each subject across time, to compute individual rates of loss, and then flowed into an average configuration using flat space warping (Fig. 5d). The resulting maps (Fig. 9) suggested dynamic loss of gray matter in superior parietal, motor and frontal brain regions (up to 5% annually). Group differences were highly significant ($p < 0.01$, *permutation test*; Fig. 9b), relative to healthy controls and non-schizophrenic controls matched for medication and IQ, and were linked with psychotic symptom severity (for details, see Thompson et al. 2001).

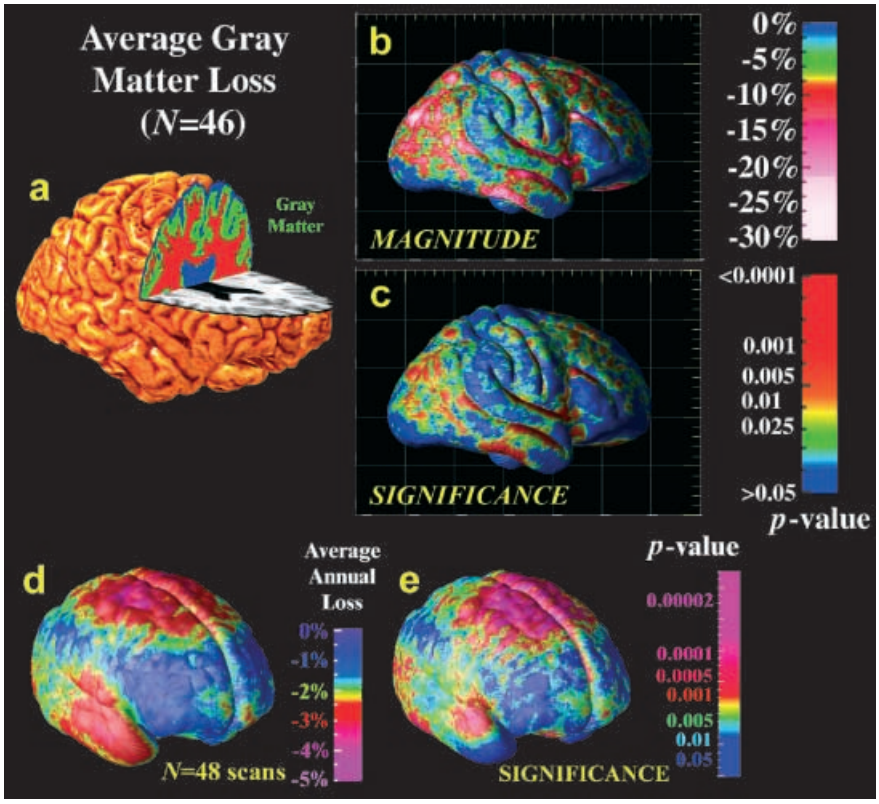

Fig. 9a–e. Average patterns of gray matter loss: Alzheimer's Disease and Schizophrenia. Scalar fields that represent the density of gray matter across the cortex (**a**) can be aligned using elastic matching of cortical patterns. A localized and highly significant loss of gray matter [(**b**), (**c**)] is revealed in temporo-parietal cortices of Alzheimer's patients relative to matched elderly controls, in a similar pattern to the metabolic and perfusion deficits seen early in the disease. If longitudinal data are available, scalar fields representing the rates of gray matter loss can also be compared. Here rates of gray matter loss (**d**) over a 5-year time span in individuals with schizophrenia are aligned and compared with corresponding dynamic maps from age-matched controls. Adolescents with schizophrenia experience statistically higher rates of loss (**e**) in motor, frontal and temporal regions

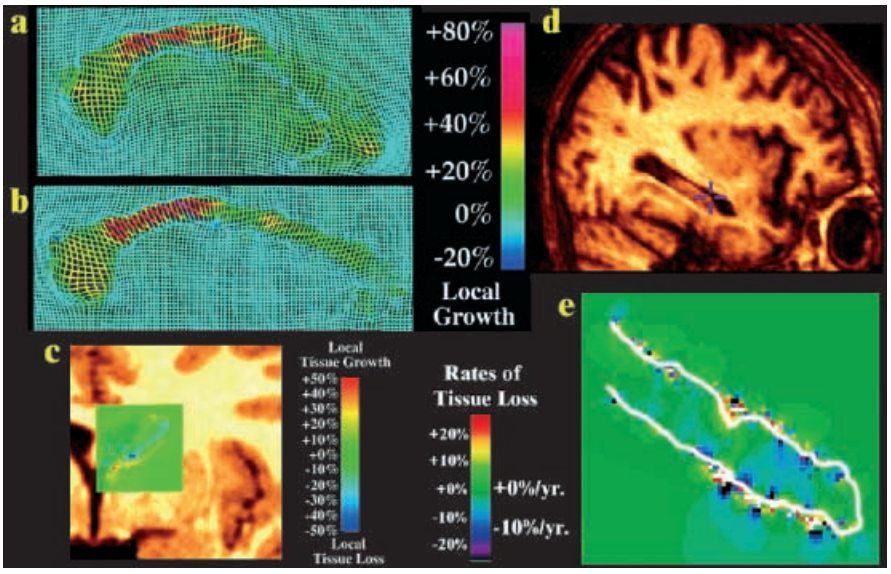

Fig. 10a–e. Tensor maps of brain change: visualizing growth and atrophy. If follow-up (longitudinal) images are available, the dynamics of brain change can be measured with tensor mapping approaches (Thompson et al. 2000). These map volumetric change at a local level, and show local rates of tissue growth or loss. Fastest growth is detected in the isthmus of the *corpus callosum* in two young girls identically scanned at ages 6 and 7 (**a**), and at ages 9 and 13 (**b**). Maps of loss rates in tissue can be generated for the developing caudate ((**c**), here in a 7–11 year old child), and for the degenerating hippocampus [(**d**),(**e**)]. In **e**, a female patient with mild Alzheimer's disease was imaged at the beginning and end of a 19 month interval with high-resolution MRI. The patient, aged 74.5 years at first scan, exhibits faster tissue loss rates in the hippocampal head (10% per year, during this interval) than in the fornix. These maps may ultimately help elucidate the dynamics of therapeutic response in an individual or a population (Thompson et al. 2000; Haney et al. 2001)

Tensor maps of brain change

Dynamic brain changes that occur over time may also be mapped by deforming a baseline scan to match a later one, and examining the warping field for growth or degenerative patterns. We recently applied these approaches to detect an anterior-to-posterior wave of growth in the brains of young children scanned repeatedly between the ages of 3 and 15 (Thompson et al. 2000). Parametric surface meshes may be built to represent anatomical structures in a series of scans over time, and these can be matched using a fully volumetric deformation. Dilation and contraction rates, and even the principal directions of growth, can be derived by examining the eigenvectors of the deformation gradient tensor, or the local Jacobian matrix of the transform that maps the earlier anatomy onto the later one (see Fig. 10). We recently applied these approaches in measuring the statistics of brain growth (Thompson et al. 2000), and tumor response to a novel chemotherapy agent, temozolomide, in an individual patient (Haney et al. 2001). By building probability densities on registered tensor fields (e.g. Thompson et al. 2000; Chung et al. 2001), a quantitative framework can be established for detecting normal and aberrant brain change, and its modulation by medication in clinical trials.

6 Genetics and brain structure

One of the most exciting frontiers of brain imaging is its linkage with genetic data in large human populations. Linking brain structure and genotype is important for understanding the (1) normal heritability of brain structure (Thompson et al. 2001), and (2) the inheritance of deficits in diseases where there are known genetic risks (e.g. Alzheimer's, schizophrenia). These studies can be set up in several ways. If a candidate marker, or risk gene, is known (e.g. apolipoprotein E, or ApoE, in Alzheimer's disease), an individual's genetic status can be used as a covariate to mine for effects of the gene on brain structure or function (Small et al. 2000). For diseases that are polygenic or where candidate markers are elusive (e.g., schizophrenia), genetic effects on brain structure may be tested using twin, familial, or discordance designs (see Lohmann et al. 1999; Thompson et al. 2001, Cannon et al. 2001 for details).

Genetic influences on brain structure

We recently developed an approach, based on cortical pattern matching (Sect. 4), to determine genetic influences on brain structure (Thompson et al. 2001). We compared the average differences in cortical gray matter density in groups of unrelated subjects, dizygotic (DZ) and monozygotic (MZ) twins. Although both types of twins share gestational and postgestational rearing environments, DZ twins share, on average, half their segregating genes, while MZ twins are normally genetically identical (with rare exceptions due to somatic mutations). Maps of intrapair gray matter differences, generated within each MZ and DZ pair, were elastically realigned for averaging across the pairs within each group, prior to intergroup comparisons. First, maps of intrapair variance and broad-sense heritability were computed using Falconer's method (Falconer 1989) to determine all genic influences on the phenotype at each cortical point (with heritability, h^2, defined as twice the difference between MZ and DZ intraclass correlation coefficients). By treating the loss of variance with increasing genetic affinity as an observation from an F-distributed random field (see Sect. 4), we identified a genetic cascade in which within-pair correlations were highest for MZ twins, lower for DZ twin pairs, and lowest of all for unrelated subjects. Specific regions of cortex were more heritable than others. We plotted these correlations across the cortex and assessed their statistical significance. This uncovered a successively increasing influence of common genetics. Genetically identical twins displayed only 10%–30% of normal differences (Fig. 11; *red and pink colors*) in a large anatomical band spanning frontal, sensorimotor, and Wernicke's language cortices. This suggests strong genetic control of brain structure in these regions. Parallel studies of heritability are also underway mapping genetic components

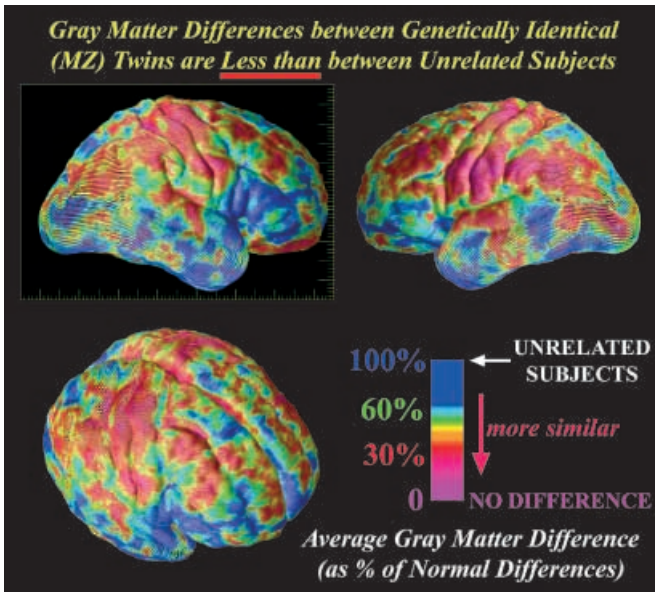

Fig. 11. Genetic influences on brain structure. Using the cortical pattern matching approaches described earlier, cortical gray matter density was determined for a database of twins scanned with MRI and compared between twins; these differences were compared with the differences observed at random between demographically pairs of age- and sex-matched individuals. Monozygotic twins, whose genes are identical (except for rare somatic mutations), were observed, on average, to have only 30%–50% of normal inter-individual differences in sensorimotor, frontal and parietal brain regions ($N = 10$ twin pairs). A statistical framework can be formulated to assess the significance of these genetic effects, and map spatial patterns of heritability (Thompson et al. 2001). Similar genetic brain maps may also uncover genetic and environmental aspects of disease (Cannon et al. 2001)

of deficits in schizophrenia (Cannon et al. 2001; cf. Styner and Gerig 2001). The resulting techniques for genetic brain mapping represent an exciting new direction in computational anatomy, and are beginning to shed light on familial liability for diseases that affect the human brain.

7 Conclusion

In this paper we presented a mathematical framework for computational anatomy. This new field in medical imaging is already uncovering fundamental features of brain structure and function in health and disease. The complexity and variability of brain data makes the reliance on brain atlases, templates, and anatomical models essential for large-scale investigations. Deformable and probabilistic atlases allow the warehousing of population-based data in a common reference 3D frame, that captures the anatomic variability using a variety of mathematical approaches. The interest in cortical anatomy, in particular, has motivated specialized approaches for analyzing its structure. Finally we suggested several new directions in computational anatomy. Dynamic and genetic brain maps, among other new techniques, are beginning to reveal how the brain develops, how diseases progress, and how genes affect complex patterns of brain structure. The resulting armory of tools shows enormous promise in shedding light on the complex structural and functional organization of the human brain.

Acknowledgements. This work was supported by research grants from the National Center for Research Resources (P41 RR13642), the National Institute of Neurological Disorders and Stroke and the National Institute of Mental Health (NINDS/NIMH NS38753), and by a *Human Brain Project* grant to the International Consortium for Brain Mapping, funded jointly by NIMH and NIDA (P20 MH/DA52176). Additional support was provided by the National Library of Medicine (LM/MH05639) and National Science Foundation (BIR 93-22434). Special thanks go to our colleagues Michael Mega, Elizabeth Sowell, Katherine Narr, Jay Giedd, Judith Rapoport, David MacDonald, Alan Evans, Ty Cannon, Roger Woods, Colin Holmes, and John Mazziotta, and many others whose support has been invaluable in these investigations.

References

1. Alouges, F.: A New Algorithm for Computing Liquid Crystal Stable Configurations: The Harmonic Mapping Case. SIAM J Num. Anal. 34(5), 1708–1726 (1997)
2. Amit, Y.: Graphical Shape Templates for Automatic Anatomy Detection with Applications to MRI Brain Scans. IEEE Trans. Med. Imag. 16(1), 28–40 (1997)
3. Amit, Y., Grenander, U., Piccioni, M.: Structural Image Restoration through Deformable Templates. J. Am. Stat. Assoc. 86(414), 376–386 (1991)
4. Andreasen, N.C., Arndt, S., Swayze, V., Cizadlo, T., Flaum, M., O'Leary, D., Ehrhardt, J.C., Yuh, W.T.C.: Thalamic Abnormalities in Schizophrenia Visualized through Magnetic Resonance Image Averaging. Science, 14 October 1994, 266, 294–298 (1994)
5. Angenent, S., Haker, S., Tannenbaum, A., Kikinis, R.: Conformal Geometry and Brain Flattening. Proc. MICCAI 1999, pp. 271–278. 1999
6. Ashburner, J., Friston, K.J.: Nonlinear spatial normalization using basis functions. Hum. Brain Mapp. 7(4), 254–266 (1999)
7. Ashburner, J., Hutton, C., Frackowiak, R., Johnsrude, I., Price, C., Friston, K.: Identifying global anatomical differences: deformation-based morphometry. Hum. Brain Mapp. 6(5/6), 348–357 (1998)
8. Ashburner, J., Neelin, P., Collins, D.L., Evans, A.C., Friston, K.J.: Incorporating Prior Knowledge into Image Registration. Neuroimage 6(4), 344–352 (1997)
9. Avoli, M., Hwa, G.C., Kostopoulos, G., Oliver, A., Villemure, J.G.: Electrophysiological Analysis of Human Neocortex in vitro: Experimental Techniques and Methodological Approaches. Can. J. Neurol. Sci. 18, 636–639 (1991)
10. Bajcsy, R., Kovacic, S.: Multiresolution Elastic Matching. Comput. Vision Graph. Image Process. 46, 1–21 (1989)
11. Berger, H.: Über das Elektroenkephalogramm des Menschen. Arch. Psychiatr. Nervenkr. 87, 527–580 (1929)
12. Bertalmio, M., Osher, S.J., Cheng, L.T., Sapiro, G.: Variational Problems and Partial Differential Equations on Implicit Surfaces: The Framework and Examples in Image Processing and Pattern Formation. UCLA CAM Report, 00(23), 2000
13. Blanton, R.E., Levitt, J.L., Thompson, P.M., Capetillo-Cunliffe, L.F., Sadoun, T., Williams, T., McCracken, J.T., Toga, A.W.: Mapping Cortical Variability and Complexity Patterns in the Developing Human Brain. Psychiatry Research 107(1), 29–43 (2001)
14. Bohm, C., Greitz, T., Kingsley, D., Berggren, B.M., Olsson, L.: Adjustable Computerized Brain Atlas for Transmission and Emission Tomography. Am. J. Neuroradiol. 4, 731–733 (1983)
15. Bookstein, F.: Principal Warps: Thin-Plate Splines and the Decomposition of Deformations, IEEE Trans. Pattern Anal. Machine Intell. 11(6), 567–585 (1989)
16. Bookstein, F.: Voxel-Based Morphometry Should Not Be Used with Imperfectly Registered Images. Neuroimage 14(6), 1454–62 (2001)
17. Bookstein, F.L.: Landmark Methods for Forms Without Landmarks: Morphometrics of Group Differences in Outline Shape. Med. Image Anal. 1(3), 225–243 (1997)
18. Brechbühler, C., Gerig, G., Kübler, O.: Parametrization of Closed Surfaces for 3D Shape Description. Comput. Vis. Image Und. 61(2), 154–170 (1995)
19. Brodmann, K.: Vergleichende Lokalisationslehre der Grosshirnrinde in ihren Prinzipien dargestellt auf Grund des Zellenbaues. Leipzig: Barth 1909. In: Some Papers on the Cerebral Cortex. Translated as: On the Comparative Localization of the Cortex, pp. 201–230. Springfield, IL: Thomas 1960

20. Bro-Nielsen, M., Gramkow, C.: Fast Fluid Registration of Medical Images. In: Höhne, K.H., Kikinis, R. (eds.): Visualization in Biomedical Computing. Lecture Notes in Computer Science, Vol. 1131, pp. 267–276. Berlin, Heidelberg, New York: Springer 1996
21. Brun, A., Englund, E.: Regional Pattern of Degeneration in Alzheimer's Disease: Neuronal Loss and Histopathologic Grading. Histopathology 5, 549–564 (1981)
22. Bullmore, E.T., Suckling, J., Overmeyer, S., Rabe-Hesketh, S., Taylor, E., Brammer, M.J.: Global, voxel, and cluster tests, by theory and permutation, for a difference between two groups of structural MR images of the brain. IEEE Trans. Med. Imag. 18, 32–42 (1999)
23. Burke, W.L.: Applied Differential Geometry. Cambridge University Press 1985
24. Cachier, P., Pennec, X., Ayache, N.: Fast Non Rigid Matching by Gradient Descent: Study and Improvements of the "Demons" Algorithm. INRIA Technical Report RR-3706, June 1999
25. Cannestra, A.F., Blood AJ., Black, K.L., Toga, A.W.: The evolution of optical signals in human and rodent cortex. Neuroimage 3, 202–208 (1996)
26. Cannestra, A.F., Santori, E.M., Holmes, C.J., Toga, A.W.: A 3D Multi-Modality Brain Map of the Nemestrina Monkey. Brain Res. Bull. 43(2), 141–148 (1998)
27. Cannon, T.D., Thompson, P.M., van Erp, T., Toga, A.W., Poutanen, V.-P., Huttunen, M., Lönnqvist, J., Standertskjöld-Nordenstam, C.-G., Narr, K.L., Beatty, J., Khaledy, M., Zoumalan, C.I., Dail, R., Kaprio, J.: Heteromodal Gray Matter Deficits in Twins Discordant for Schizophrenia Isolated Using Cortical Pattern Matching. 31st International Meeting of the Society for Neuroscience, San Diego, CA, November 10–15, 2001
28. Cao, J., Worsley, K.J.: The Geometry of the Hotelling's T-squared Random Field with Applications to the Detection of Shape Changes. Ann. Stat. 27, 925–942 (2001)
29. Christensen, G.E., Johnson, H.J., Haller, J.W., Melloy, J., Vannier, M.W., Marsh, J.L.: Synthesizing average 3D anatomical shapes using deformable templates. In: Hanson, K.M. (ed.): Image Processing. Proc. SPIE Medical Imaging, Vol. 3661. 1999
30. Christensen, G.E., Miller, M.I., Marsh, J.L., Vannier, M.W.: Automatic Analysis of Medical Images using a Deformable Textbook. Proc. Comp. Assist. Radiol. 1995, pp. 152–157. Berlin, Heidelberg, New York: Springer 1995
31. Christensen, G.E., Rabbitt, R.D., Miller, M.I.: A Deformable Neuroanatomy Textbook based on Viscous Fluid Mechanics. 27th Ann. Conf. on Inf. Sciences and Systems, pp. 211–216, 1993
32. Christensen, G.E., Rabbitt, R.D., Miller, M.I.: Deformable Templates using Large Deformation Kinematics. IEEE Trans. Image Process. 5(10), 1435–1447 (1996)
33. Christensen, G.E., Rabbitt, R.D., Miller, M.I., Joshi, S.C., Grenander, U., Coogan, T.A., Van Essen, D.C.: Topological Properties of Smooth Anatomic Maps. In: Bizais, Y., Barillot, C., Di Paola, R. (eds.): Information Processing in Medical Imaging, pp. 101–112. 1995
34. Chung, M.K., Worsley, K.J., Paus, T., Cherif, C., Collins, D.L., Giedd, J.N., Rapoport, J.L., Evans, A.C.: A Unified Statistical Approach to Deformation-Based Morphometry. Neuroimage 14, 595–606 (2001)
35. Chung, M.K., Worsley, K.J., Taylor, J., Ramsay, J., Robbins, S., Evans, A.C.: Diffusion Smoothing on the Cortical Surface. Proc. Hum. Brain Mapp., (2000)
36. Collins, D.L., Holmes, C.J., Peters, T.M., Evans, A.C.: Automatic 3D Model-Based Neuroanatomical Segmentation. Hum. Brain Mapp. 3, 190–208 (1995)
37. Collins, D.L., Peters, T.M., Evans, A.C.: An Automated 3D Non-Linear Image Deformation Procedure for Determination of Gross Morphometric Variability in the Human Brain. Proc. Visual. Biomed. Comp. (SPIE) 3, 180–190 (1994)
38. Cootes, T.F., Taylor, C.J., Cooper, D.H., Graham, J.: Active shape models – their training and application. Comp. Vis. Image Und. 61(1), 38–59 (1995)
39. Csernansky, J.G., Joshi, S., Wang, L., Haller, J.W., Gado, M., Miller, J.P., Grenander, U., Miller, M.I.: Hippocampal morphometry in schizophrenia by high dimensional brain mapping. Proc. Natl. Acad. Sci. USA, 1998 Sep. 15, 95(19), 11 406–11 411 (1998)
40. Damasio, H.: Human Brain Anatomy in Computerized Images. Oxford, New York: Oxford University Press 1995
41. Davatzikos, C.: Spatial Normalization of 3D Brain Images using Deformable Models. J. Comput. Assist. Tomogr. 20(4), 656–665 (1996a)
42. Davatzikos, C., Vaillant, M., Resnick, S.M., Prince, J.L., Letovsky, S., Bryan, R.N.: A Computerized Approach for Morphological Analysis of the Corpus Callosum, J. Comput. Assist. Tomogr. 20(1), 88–97 (1996b)
43. Davidson, R.J., Hugdahl, K.: Brain Asymmetry. Cambridge, MA, USA: MIT Press 1994
44. Davis, M.H., Khotanzad, A., Flamig, D.P.: 3D Image Matching Using a Radial Basis Function Neural Network. Proc. 1996 World Congress on Neural Networks, San Diego, California, Sept. 15–18, 1996. pp. 1174–1179. 1996
45. Davis, M.H., Khotanzad, A., Flamig, D.P., Harms, S.E.: A Physics Based Coordinate Transformation for 3D Image Matching. IEEE Trans. Med. Imag. 16(3), 317–328 (1997)
46. Dawant, B.M., Thirion, J.-P., Maes, F., Vandermeulen, D., Demaerel, P.: Automatic 3D segmentation of internal structures of the head in MR images using a combination of similarity and free form transformation. In: Proc. SPIE Med. Imag. 1998. Image Process. 3338, 545–554 (1998)
47. Dengler, J., Schmidt, M.: The Dynamic Pyramid – A Model for Motion Analysis with Controlled Continuity. Int. J. Patt. Recogn. Artif. Intell. 2(2), 275–286 (1988)
48. Dinov, I.D., Thompson, P.M., Woods, R.P., Mega, M.S., Holmes, C.J., Sumners, D., Saxena, S., Toga, A.W.: Probabilistic Sub-Volume Partitioning Techniques for Determining the Statistically Significant Regions of Activation in Stereotaxic Functional Data. J. Comput. Assist. Tomogr. 24(1), 128–138 (2000)
49. Downs, J., Lancaster, J.L., Fox, P.T.: 3D Surface-Based Normalization using a Convex Hull, In: Thatcher, R., Hallett, M., Zeffiro, T., John, E., Huerta, M. (eds.): Functional Neuroimaging: Technical Foundations, pp. 63–80. San Diego, CA, USA: Academic Press 1994
50. Drury, H.A., Van Essen, D.C.: Analysis of Functional Specialization in Human Cerebral Cortex using the Visible Man Surface Based Atlas. Hum. Brain Mapp. 5, 233–237 (1997)
51. Dupuis, P., Grenander, U., Miller, M.I.: Variational problems on flows of diffeomorphisms for image matching. Quarterly Appl. Math. 56(3), 587–600 (1998)
52. Duvernoy, H.M.: The Human Brain. Berlin, Heidelberg, New York: Springer 1991
53. Evans, A.C., Collins, D.L., Neelin, P., MacDonald, D., Kamber, M., Marrett, T.S.: Three-Dimensional Correlative Imaging: Applications in Human Brain Mapping. In: Thatcher, R.W., Hallett, M., Zeffiro, T., John, E.R., Huerta, M. (eds.): Functional Neuroimaging: Technical Foundations, pp. 145–162. San Diego, CA, USA: Academic Press 1994
54. Evans, A.C., Dai, W., Collins, D.L., Neelin, P., Marrett, S.: Warping of a Computerized 3D Atlas to Match Brain Image Volumes for Quantitative. Neuroanatomical and Functional Analysis, SPIE Medical Imaging 1445, 236–247 (1991)
55. Falconer, D.S.: Introduction to Quantitative Genetics. 3rd edn. Essex, UK: Longman 1989
56. Fischl, B., Sereno, M.I., Tootell, R.B.H., Dale, A.M.: High-Resolution Inter-Subject Averaging and a Coordinate System for the Cortical Surface. Hum. Brain Mapp. 8(4), 272–284 (1999)
57. Fishman, E.K.: High resolution three-dimensional imaging from subsecond helical CT datasets. Applications in vascular imaging. AJR 169, 441–443 (1997)
58. Frackowiak, R.S.J., Friston, K.J., Frith, C.D., Dolan, R.J., Mazziotta, J.C.: Human Brain Function. Academic Press 1997
59. Freeborough, P.A., Fox, N.C.: Modeling brain deformations in Alzheimer disease by fluid registration of serial 3D MR images. J. Comput. Assist. Tomogr. 22(5), 838–843 (1998)
60. Gaser, C., Kiebel, S., Riehemann, S., Volz, H.-P., Sauer, H.: Statistical parametric mapping of structural changes in brain – Application to schizophrenia research. Poster #0718, 4th Int. Conf. on Functional Mapping of the Human Brain, Montreal, 1998
61. Ge, Y., Fitzpatrick, J.M., Kessler, R.M., Jeske-Janicka, M.: Intersubject Brain Image Registration using both Cortical and Subcortical Landmarks. SPIE Image Process. 2434, 81–95 (1995)
62. Gee, J.C., Bajcsy, R.K.: Elastic Matching: Continuum-Mechanical and Probabilistic Analysis: in: Toga, A.W. (ed.): Brain Warping. San Diego: Academic Press 1998
63. Gee, J.C., Le Briquer, L.: An Empirical Model of Brain Shape. Maximum Entropy and Bayesian Methods. Aug. 4–8, 1997
64. Gee, J.C., LeBriquer, L., Barillot, C., Haynor, D.R., Bajcsy, R.: Bayesian Approach to the Brain Image Matching Problem. Inst. for Res. in Cogn. Sci., Technical Report 95–08, April 1995

65. Gee, J.C., Reivich M., Bajcsy, R.: Elastically Deforming an Atlas to Match Anatomical Brain Images. J. Comput. Assist. Tomogr. 17(2), 225–236 (1993)
66. Geschwind, N., Levitsky, W.: Human Brain: Left-Right Asymmetries in Temporal Speech Region. Science 161, 186 (1968)
67. Geyer, S., Schleicher, A., Zilles, K.: The Somatosensory Cortex of Man: Cytoarchitecture and Regional Distributions of Receptor Binding Sites. Neuroimage 6(1), 27–45 (1997)
68. Giedd, J.N., Blumenthal, J., Jeffries, N.O., Castellanos, F.X., Liu, H., Vaituzis, A.C., Fernandez, T., Zijdenbos, A., Paus, T., Evans, A.C., Rapoport, J.L.: Brain development during childhood and adolescence: a longitudinal MRI study. Nature Neuroscience 2(10), 861–863 (1999)
69. Gramkow, C.: Registration of 2D and 3D Medical Images: M.Sc. Thesis, Denmark Tech. Univ., 1996
70. Gramkow, C., Bro-Nielsen, M.: Comparison of Three Filters in the Solution of the Navier–Stokes Equation in Registration. Proc. Scandinavian Conference on Image Analysis (SCIA'97), pp. 795–802. 1997
71. Grenander, U.: Pattern Synthesis: Lectures in Pattern Theory. Appl. Math. Sci., Vol. 13. Berlin, Heidelberg, New York: Springer 1976
72. Grenander, U., Miller, M.I.: Representations of Knowledge in Complex Systems, J. R. Stat. Soc. B. 56(4), 549–603 (1994)
73. Grenander, U., Miller, M.I.: Computational Anatomy: An Emerging Discipline. Technical Report, Dept. of Mathematics, Brown University, 1998
74. Guimond, A., Meunier, J., Thirion, J.-P. (1999). Average Brain Models: A Convergence Study. INRIA Technical Report RR-3731, July 1999
75. Haller, J.W., Banerjee, A., Christensen, G.E., Gado, M., Joshi, S., Miller, M.I., Sheline, Y., Vannier, M.W., Csernansky, J.G.: Three-Dimensional Hippocampal MR Morphometry with High-Dimensional Transformation of a Neuroanatomic Atlas. Radiology 202(2), 504–510 (1997)
76. Haney, S., Thompson, P.M., Cloughesy, T.F., Alger, J.R., Frew, A., Torres-Trejo, A., Mazziotta, J.C., Toga, A.W.: Mapping Response in a Patient with Malignant Glioma. J. Comput. Assist. Tomogr. 25(4), 529–536 (2001)
77. Holmes, A.P., Blair, R.C., Watson, J.D.G., Ford, I.: Nonparametric analysis of statistic images from functional mapping experiments. J. Cereb. Blood Flow Metab. 16(1), 7–22 (1996)
78. Holmes, C.J., Hoge, R., Collins, L., Woods, R., Toga, A.W., Evans, A.C.: Enhancement of MR images using registration for signal averaging. J. Comput. Assist. Tomogr. 22(2), 324–333 (1998)
79. Hounsfield, G.N.: Computerized Transverse Axial Scanning (tomography). I. Description of System. Br. J. Radiol. 46, 1016–1022 (1973)
80. Hurdal, M.K., Sumners, D.L., Stephenson, K., Bowers, P.L., Rottenberg, D.A.: Circlepack: Software for creating quasi-conformal flat maps of the brain, pp. S250. Fifth International Conference on Functional Mapping of the Human Brain, 1999
81. Ingvar, M., Eriksson, L., Greitz, T., Stoneelander, S. et al.: Methodological Aspects of Brain Activation Studies – Cerebral Blood Flow Determined with [O-15]-Butanol and Positron Emission Tomography. J. Cereb. Blood Flow Metab. 14(4), 628–638 (1994)
82. Iosifescu, D.V., Shenton, M.E., Warfield, S.K., Kikinis, R., Dengler, J., Jolesz, F.A., McCarley, R.W.: An Automated Registration Algorithm for Measuring, MRI Subcortical Brain Structures. Neuroimage 6(1), 13–25 (1997)
83. Jacobs, R.E., Fraser, S.E.: Magnetic Resonance Microscopy of Embryonic Cell Lineages and Movements. Science 263(5147), 681–684 (1994)
84. Joshi, S., Miller, M.I., Grenander, U.: On the Geometry and Shape of Brain Sub-Manifolds. Int. J. Patt. Recogn. Artif. Intell. 11, 8 (1998)
85. Joshi, S.C., Miller, M.I., Christensen, G.E., Banerjee, A., Coogan, T.A., Grenander, U.: Hierarchical Brain Mapping via a Generalized Dirichlet Solution for Mapping Brain Manifolds. Proc. SPIE Conference on Optical Science, Engineering and Instrumentation, San Diego, CA, Aug. 1995. Vision Geometry IV 2573, 278–289 (1995)
86. Kass, M., Witkin, A., Terzopoulos, D.: Snakes: active contour models. In: First International Conference on Computer Vision, pp. 259–268. 1987
87. Kennedy, D.N., Lange, N., Makris, N., Bates, J., Meyer, J., Caviness, V.S. Jr.: Gyri of the human neocortex: an MRI-based analysis of volume and variance. Cereb. Cortex 8(4), 372–384 (1998)
88. Kikinis, R., Shenton, M.E., Gerig, G., Hokama, H., Haimson, J., O'Donnell, B.F., Wible, C.G., McCarley, R.W., Jolesz, F.A.: Temporal Lobe Sulco-Gyral Pattern Anomalies in Schizophrenia: An in vivo MR Three-Dimensional Surface Rendering Study. Neurosci. Lett. 182, 7–12 (1994)
89. Kikinis, R., Shenton, M.E., Iosifescu, D.V., McCarley, R.W., Saiviroonporn, P., Hokama, H.H., Robatino, A., Metcalf, D., Wible, C.G., Portas, C.M., Donnino, R., Jolesz, F.: A Digital Brain Atlas for Surgical Planning, Model-Driven Segmentation, and Teaching. IEEE Trans. Visual. Comput. Graph. 2(3), 232–241 (1996)
90. Kim, B., Boes, J.L., Frey, K.A., Meyer, C.R.: Mutual Information for Automated Unwarping of Rat Brain Autoradiographs. Neuroimage 5(1), 31–40 (1997)
91. Kochunov, P., Lancaster, J., Thompson, P.M., Toga, A.W., Brewer, P., Hardies, J., Fox, P.T.: An Optimized Individual Target Brain in the Talairach Coordinate System. J. Comput. Assist. Tomogr. (2002). In press
92. Kochunov, P., Lancaster, J., Thompson, P.M., Woods, R.P., Hardies, J., Fox, P.T.: Regional Spatial Normalization: Towards an Optimal Target. J. Comput. Assist. Tomogr. 25(5), 805–816 (2001)
93. Krzanowski, W.J.: Principles of Multivariate Analysis: A User's Perspective. Oxford, England: Clarendon Press 1988
94. Lauterbur, P.: Image formation by induced local interactions: Examples employing nuclear magnetic resonance. Nature 242, 190–191 (1973)
95. Le Bihan, D.: Functional MRI of the Brain: Principles, Applications and Limitations. Neuroradiol. 23(1), 1–5 (1996)
96. Le Goualher, G., Procyk, E., Collins, D.L., Venugopal, R., Barillot, C., Evans, A.C.: Automated extraction and variability analysis of sulcal neuroanatomy. IEEE Trans. Med. Imag. 18(3), 206–217 (1999)
97. Leonard, C.M.: Structural Variation in the Developing and Mature Cerebral Cortex: Noise or Signal? In: Thatcher, R.W., Reid Lyon, G., Rumsey, J., Krasnegor, N. (eds.): Developmental Neuroimaging: Mapping the Development of Brain and Behavior, pp. 207–231. San Diego, CA, USA: Academic Press 1996
98. Lester, H., Arridge, S.R., Jansons, K.M., Lemieux, L., Hajnal, J.V., Oatridge, A.: Non-linear registration with the variable viscosity fluid algorithm. 16th Int. Conf. on Info. Proc. in Med. Imaging, IPMI'99. 1999
99. Liseikin, V.D.: On a Variational Method for Generating Adaptive Grids on N-Dimensional Surfaces. Doklady Akademii Nauk. CCCP 319(3), 546–549 (1991)
100. Lohmann, G., von Cramon, D.Y.: Automatic labelling of the human cortical surface using sulcal basins. Med. Image Anal. 4(3), 179–188 (2000)
101. Lohmann, G., von Cramon, D.Y., Steinmetz, H.: Sulcal variability of twins. Cereb. Cortex 9(7), 754–63 (1999)
102. MacDonald, D.: A Method for Identifying Geometrically Simple Surfaces from Three Dimensional Images. PhD Thesis, McGill Univ., Canada, 1998
103. Mai, J., Assheuer, J., Paxinos, G.: Atlas of the Human Brain. San Diego, CA, USA: Academic Press 1997
104. Maintz, J.B., Viergever, M.A.: A survey of medical image registration. Med. Image Anal. 2(1), 1–36 (1998)
105. Manceaux-Demiau, A., Bryan, R.N., Davatzikos, C.: A Probabilistic Ribbon Model for Shape Analysis of the Cerebral Sulci: Application to the Central Sulcus. J. Comput. Assist. Tomogr. 22(6), 962–971 (1998)
106. Mangin, J.-F., Frouin, V., Bloch, I., Régis, J., Lopez-Krahe, J.: Automatic Construction of an Attributed Relational Graph Representing the Cortex Topography using Homotopic Transformations. SPIE 2299, 110–121 (1994)
107. Martin, J.: Characterization of Neuropathological Shape Deformations. PhD Thesis, Radiological Sciences Program, MIT Dept. Nuclear Engineering, 1995
108. Mazziotta, J.C., Toga, A.W., Evans, A.C., Fox, P., Lancaster, J.: A Probabilistic Atlas of the Human Brain: Theory and Rationale for its Development. Neuroimage 2, 89–101 (1995)
109. Mazziotta, J.C., Toga, A.W., Evans, A.C., Fox, P.T., Lancaster, J., Zilles, K., Woods, R.P., Paus, T., Simpson, G., Pike, B., Holmes, C.J., Collins, D.L., Thompson, P.M., MacDonald, D., Schormann, T., Amunts, K., Palomero-Gallagher, N., Parsons, L., Narr, K.L., Kabani, N., Le Goualher, G., Boomsma, D., Cannon, T., Kawashima, R., Mazoyer, B.: A Probabilistic Atlas and Reference System for the Human Brain. J. R. Soc. 356(1412), 1293–1322 (2001)
110. Mega, M.S., Chu, T., Mazziotta, J.C., Trivedi, K.H., Thompson, P.M., Shah, A., Cole, G., Frautschy, S.A., Toga, A.W.: Mapping Biochemistry to Metabolism: FDG-PET and Beta-Amyloid Burden in Alzheimer's Disease. Neuroreport 10(14), Sept. 29, 2911–2917 (1999)
111. Mega, M.S., Thompson, P.M., Cummings, J.L., Back, C.L., Xu, L.Q., Zohoori, S., Goldkorn, A., Moussai, J., Fairbanks, L., Small, G.W.,

Toga, A.W.: Sulcal Variability in the Alzheimer's Brain: Correlations with Cognition. Neurology 50, 145–151 (1998)
112. Mega, M.S., Thompson, P.M., Toga, A.W., Cummings, J.L.: Brain Mapping in Dementia. Book Chapter in: Toga, A.W., Mazziotta, J.C. (eds.): Brain Mapping: The Disorders. San Diego, CA, USA: Academic Press 2000
113. Mega, M.S., Woods, R.P., Thompson, P.M., Dinov, I.D., Lee, L., Aron, J., Zoumalan, C.I., Cummings, J.L., Toga, A.W.: Detecting Metabolic Patterns Associated with Minimal Cognitive Impairment using FDG-PET Analysis within a Probabilistic Brain Atlas based upon Continuum Mechanics. Proc. Soc. Neurosci., (1998)
114. Megalooikonomou, V.M., Ford, J., Shen, L., Makedon, F., Saykin, A.: Data Mining in Brain Imaging. Stat. Methods Med. Res. 9, 359–394 (2000)
115. Miller, M.I., Christensen, G.E., Amit, Y., Grenander, U.: Mathematical Textbook of Deformable Neuroanatomies. Proc. Nat. Acad. Sci. USA 90, 11 944–11 948 (1993)
116. Miller, M.I., Younes, L.: Group actions, homeomorphisms, and matching: a general framework, Technical Report, 1999. Available at: http://www.cmla.ens-cachan.fr/Utilisateurs/younes/
117. Minoshima, S., Koeppe, R.A., Frey, K.A., Ishihara, M., Kuhl, D.E.: Stereotactic PET Atlas of the Human Brain: Aid for Visual Interpretation of Functional Brain Images. J. Nucl. Med. 35, 949–954 (1994)
118. Monga, O., Benayoun, S.: Using Partial Derivatives of 3D Images to Extract Typical Surface Features. Comput. Visual. Imag. Und. 61(2), 171–189 (1995)
119. Mori, S., Itoh, R., Zhang, J., Kaufmann, W.E., van Zijl, P.C., Solaiyappan, M., Yarowsky, P.: Diffusion tensor imaging of the developing mouse brain. Magn. Reson. Med. 46(1), 18–23 (2001)
120. Moshfeghi, M., Raganath, S., Nawyn, K.: 3D Elastic Matching of Volumes. IEEE Trans. Image Process. 3(2), 128–138 (1994)
121. Narr, K.L., Thompson, P.M., Sharma, T., Moussai, J., Blanton, R.E., Anvar, B., Edris, A., Krupp, R., Rayman, J., Toga, A.W.: 3D Shape Characterization and Mapping of Temporo-Limbic Regions and the Lateral Ventricles in Schizophrenia. Biol. Psychiatry 50, 84–97 (2001)
122. Narr, K.L., Thompson, P.M., Sharma, T., Moussai, J., Cannestra, A.F., Toga, A.W.: Mapping Corpus Callosum Morphology in Schizophrenia. Cereb. Cortex 10(1), 40–49 (2000)
123. Narr, K.L., Thompson, P.M., Sharma, T., Moussai, J., Zoumalan, C.I., Rayman, J., Toga, A.W.: 3D Mapping of Gyral Shape and Cortical Surface Asymmetries in Schizophrenia: Gender Effects. Am. J. Psychiatry 158(2), 244–255 (2001)
124. Nestor, P.G., Shenton, M.E., McCarley, R.W., Haimson, J., Smith, R.S., O'Donnell, B., Kimble, M., Kikinis, R., Jolesz, F.A.: Neuropsychological correlates of MRI temporal lobe abnormalities in schizophrenia. Am. J. Psychiatry 150(12), 1849–1855 (1993)
125. Nielsen, M., Florack, L., Deriche, R.: Regularization and Scale Space. INRIA Tech. Rep. RR-2352, Sept. 1994
126. Ono, M., Kubik, S., Abernathey, C.D.: Atlas of the Cerebral Sulci. Stuttgart: Thieme 1990
127. Palovcik, R.A., Reid, S.A., Principe, J.C., Albuquerque, A.: 3D Computer Animation of Electrophysiological Responses. J. Neurosci. Methods 41, 1–9 (1992)
128. Paus, T., Tomaioulo, F., Otaky, N., MacDonald, D., Petrides, M., Atlas, J., Morris, R., Evans, A.C.: Human Cingulate and Paracingulate Sulci: Pattern, Variability, Asymmetry and Probabilistic Map. Cereb. Cortex 6, 207–214 (1996)
129. Paus, T., Zijdenbos, A., Worsley, K., Collins, D.L., Blumenthal, J., Giedd, J.N., Rapoport, J.L., Evans, A.C.: Structural maturation of neural pathways in children and adolescents: in vivo study. Science 283(5409), 1908–1911 (1999)
130. Penfield, W., Boldrey, E.: Somatic Motor and Sensory Representation in the Cerebral Cortex of Man as Studied by Electrical Stimulation. Brain 60, 389–443 (1937)
131. Polyakov, A.M.: Gauge Fields and Strings. New York: Harwood 1987
132. Rademacher, J., Caviness, V.S. Jr, Steinmetz, H., Galaburda, A.M.: Topographical Variation of the Human Primary Cortices: Implications for Neuroimaging, Brain Mapping and Neurobiology. Cereb. Cortex 3(4), 313–329 (1993)
133. Régis, J.: Anatomie sulcale profonde et cartographie fonctionnelle du cortex cérébral. PhD Thesis, University of Marseille, 1994. In French
134. Rettmann, M.E., Han, X., Prince, J.L.: Watersheds on the Cortical Surface for Automated Sulcal Segmentation. IEEE Workshop on Mathematical Methods in Biomedical Image Analysis, June 2000, pp. 20–27
135. Ripley, B.D.: Pattern Recognition and Neural Networks. Cambridge Univ. Press 1996
136. Rizzo, G., Gilardi, M.C., Prinster, A., Grassi, F., Scotti, G., Cerutti, S., Fazio, F.: An Elastic Computerized Brain Atlas for the Analysis of Clinical PET/SPET Data. Eur. J. Nucl. Med. 22(11), 1313–1318 (1995)
137. Sapiro, G.: Geometric Partial Differential Equations and Image Processing. Cambridge University Press 2001
138. Sarrut, D.: Recalage multi-modal et plate-forme à accès distant pour l'imagerie médicale, PhD thesis, Université Lumière, Lyon, 2000
139. Schmahmann, J.D., Doyon, J., McDonald, D., Holmes, C., Lavoie, K., Hurwitz, A.S., Kabani, N., Toga, A., Evans, A., Petrides, M.: 3D MRI atlas of the human cerebellum in proportional stereotaxic space. Neuroimage. 10(3 Pt 1), 233–260 (1999)
140. Schormann, T., Henn, S., Zilles, K.: A New Approach to Fast Elastic Alignment with Applications to Human Brains. Proc. Visualization in Biomed. Comp. 4, 337–342 (1996)
141. Sebastian, T.B., Klein, P.N., Kimia, B.B., Crisco, J.J.: Constructing 2D Curve Atlases. Proc. IEEE Workshop on Mathematical Methods in Biomedical Image Analysis (MMBIA'00), 2000
142. Shattuck, D., Leahy, R.M.: Topological refinement of volumetric data. Proc. SPIE Medical Imaging Conference Proceedings. SPIE 3661, 204–213 (1999)
143. Small, G.W., Ercoli, L.M., Silverman, D.H., Huang, S.C., Komo, S., et al.: Cerebral metabolic and cognitive decline in persons at genetic risk for Alzheimer's disease. Proc. Natl. Acad. Sci. USA, 2000 May 23, 97(11), 6037–6042 (2000)
144. Smith, G.E.: A New Topographical Survey of the Human Cerebral Cortex, being an Account of the Distribution of the Anatomically Distinct Cortical Areas and their Relationship to the Cerebral Sulci. J. Anatomy 41, 237–254 (1907)
145. Sowell, E.R., Levitt, J., Thompson, P.M., Holmes, C.J., Blanton, R.E., Kornsand, D.S., Caplan, R., McCracken, J., Asarnow, R., Toga, A.W.: Brain Abnormalities in Early-Onset Schizophrenia Spectrum Disorder Observed with Statistical Parametric Mapping of Structural Magnetic Resonance Images. Am. J. Psychiatry 157(9), 1475–1484 (2001)
146. Sowell, E.R., Mattson, S.N., Thompson, P.M., Jernigan, T.L., Riley, E.P., Toga, A.W.: Mapping Corpus Callosum Morphology and its Neurocognitive Correlates: The Effects of Prenatal Alcohol Exposure. Neurology 57(2), 235–244 (2001)
147. Sowell, E.R., Thompson, P.M., Holmes, C.J., Batth, R., Trauner, D.A., Jernigan, T.L., Toga, A.W.: Localizing Age-Related Changes in Brain Structure between Childhood and Adolescence using Statistical Parametric Mapping. Neuroimage 9(6 pt 1), 587–597 (1999)
148. Sowell, E.R., Thompson, P.M., Holmes, C.J., Jernigan, T.L., Toga, A.W.: Progression of Structural Changes in the Human Brain during the First Three Decades of Life: In Vivo Evidence for Post-Adolescent Frontal and Striatal Maturation. Nature Neurosci. 2(10), 859–861 (1999)
149. Sowell, E.R., Thompson, P.M., Mega, M.S., Zoumalan, C.I., Lindshield, C., Rex, D.E., et al.: Gyral Pattern Delineation in 3D: Surface Curve Protocol. 2000. Available via Internet: http://www.loni.ucla.edu/~esowell/new_sulcvar.html
150. Sowell, E.R., Thompson, P.M., Rex, D.E., Kornsand, D.S., Jernigan, T.L., Toga, A.W.: Mapping Sulcal Pattern Asymmetry and Cortical Gray Matter Thickness In Vivo: Maturation of Posterior Perisylvian Cortices. Cerebral Cortex 12(1), 17–26 (2001)
151. Sowell, E.R., Thompson, P.M., Tessner, K.D., Toga, A.W.: Accelerated Brain Growth and Cortical Gray Matter Thinning are Inversely Related during Post-Adolescent Frontal Lobe Maturation. J. Neurosci. 21(22), 8819–8829 (2001)
152. Spitzer, V., Ackerman, M.J., Scherzinger, A.L., Whitlock, D.: The Visible Human Male: A Technical Report, J. Am. Med. Informatics Assoc. 3(2), 118–130 (1996). http://www.nlm.nih.gov/extramural_research.dir/visible_human.html
153. St-Jean, P., Sadikot, A.F., Collins, L., Clonda, D., Kasrai, R., Evans, A.C., Peters, T.M.: Automated atlas integration and interactive three-dimensional visualization tools for planning and guidance in functional neurosurgery. IEEE Trans. Med. Imag. 17(5), 672–680 (1998)
154. Strauss, E., Kosaka, B., Wada, J.: The Neurobiological Basis of Lateralized Cerebral Function. A Review. Hum. Neurobiol. 2(3), 115–127 (1983)
155. Styner, M., Gerig, G.: Medial models incorporating object variability for 3D shape analysis. Proc. IPMI, UC Davis, pp. 502–516. 2001

156. Subsol, G.: Construction automatique d'atlas anatomiques morphométriques à partir d'images médicales tridimensionnelles. PhD thesis, École Centrale Paris, 1995
157. Subsol, G., Roberts, N., Doran, M., Thirion, J.P., Whitehouse, G.H.: Automatic Analysis of Cerebral Atrophy. Magn. Reson. Imaging 15(8), 917–927 (1997)
158. Swanson, L.W.: Brain Maps: Structure of the Rat Brain. Amsterdam: Elsevier Science 1992
159. Szeliski, R., Lavallée, S.: Matching 3D Anatomical Surfaces with Non-Rigid Deformations using Octree-Splines. SPIE, Vol. 2031, Geometric Methods in Computer Vision II, pp. 306–315. 1993
160. Talairach, J., Tournoux, P.: Co-planar Stereotaxic Atlas of the Human Brain. New York: Thieme 1988
161. Tao, X., Han, X., Rettmann, M.E., Prince, J.L., Davatzikos, C.: Statistical Study on Cortical Sulci of Human Brains. Proc. 17th Information Processing in Medical Imaging (IPMI), June 2001
162. Thirion, J.-P.: Fast Non-Rigid Matching of Medical Images. INRIA Internal Report 2547, Projet Epidaure, INRIA, France, 1995
163. Thirion, J.-P., Prima, S., Subsol, S.: Statistical Analysis of Dissymmetry in Volumetric Medical Images. Med. Image Anal. 4(2), 111–121 (2000)
164. Thompson, P.M., Cannon, T.D., Narr, K.L., van Erp, T., Khaledy, M., Poutanen, V.-P., Huttunen, M., Lönnqvist, J., Standertskjöld-Nordenstam, C.-G., Kaprio, J., Dail, R., Zoumalan, C.I., Toga, A.W.: Genetic Influences on Brain Structure. Nature Neurosci. 4(12), 1253–1258 (2001)
165. Thompson, P.M., Giedd, J.N., Woods, R.P., MacDonald, D., Evans, A.C., Toga, A.W.: Growth Patterns in the Developing Brain Detected By Using Continuum-Mechanical Tensor Maps. Nature 404(6774), 190–193 (2000)
166. Thompson, P.M., MacDonald, D., Mega, M.S., Holmes, C.J., Evans, A.C., Toga, A.W.: Detection and Mapping of Abnormal Brain Structure with a Probabilistic Atlas of Cortical Surfaces. J. Comput. Assist. Tomogr. 21(4), 567–581 (1997)
167. Thompson, P.M., Mega, M.S., Narr, K.L., Sowell, E.R., Blanton, R.E., Toga, A.W.: Brain Image Analysis and Atlas Construction, Invited Chapter. In: Fitzpatrick, M. (ed.): SPIE Handbook on Medical Image Analysis. Society of Photo-Optical Instrumentation Engineers (SPIE) Press, August 2000
168. Thompson, P.M., Mega, M.S., Toga, A.W.: Disease-Specific Brain Atlases. Chapter in: Toga, A.W., Mazziotta, J.C. (eds.): Brain Mapping: The Disorders. San Diego, CA, USA: Academic Press 2000
169. Thompson, P.M., Mega, M.S., Vidal, C., Rapoport, J.L., Toga, A.W.: Detecting Disease-Specific Patterns of Brain Structure using Cortical Pattern Matching and a Population-Based Probabilistic Brain Atlas. IEEE Conference on Information Processing in Medical Imaging (IPMI), UC Davis, 2001
170. Thompson, P.M., Mega, M.S., Woods, R.P., Blanton, R.E., Moussai, J., Zoumalan, C.I., Aron, J., Cummings, J.L., Toga, A.W.: Cortical Change in Alzheimer's Disease Detected with a Disease-Specific Population-Based Brain Atlas. Cereb. Cortex 11(1), 1–16 (2001)
171. Thompson, P.M., Moussai, J., Khan, A.A., Zohoori, S., Goldkorn, A., Mega, M.S., Small, G.W., Cummings, J.L., Toga, A.W.: Cortical Variability and Asymmetry in Normal Aging and Alzheimer's Disease. Cereb. Cortex 8(6), 492–509 (1998)
172. Thompson, P.M., Schwartz, C., Lin, R.T., Khan, A.A., Toga, A.W.: 3D Statistical Analysis of Sulcal Variability in the Human Brain. J. Neurosci. 16(13), 4261–4274 (1996)
173. Thompson, P.M., Schwartz, C., Toga, A.W.: High-Resolution Random Mesh Algorithms for Creating a Probabilistic 3D Surface Atlas of the Human Brain. Neuroimage 3(1), 19–34 (1996)
174. Thompson, P.M., Toga, A.W.: A Surface-Based Technique for Warping 3-Dimensional Images of the Brain. IEEE Trans. Med. Imag., Aug. 1996, 15(4), 1–16 (1996)
175. Thompson, P.M., Toga, A.W.: Detection, Visualization and Animation of Abnormal Anatomic Structure with a Deformable Probabilistic Brain Atlas based on Random Vector Field Transformations. Med. Image Anal. 1(4), 271–294 (1997)
176. Thompson, P.M., Toga, A.W.: Anatomically-Driven Strategies for High-Dimensional Brain Image Warping and Pathology Detection. In: Toga, A.W. (ed.): Brain Warping, pp. 311–336. Academic Press 1998
177. Thompson, P.M., Toga, A.W.: Elastic Image Registration and Pathology Detection, Book Chapter. In: Bankman, I., Rangayyan, R., Evans, A.C., Woods, R.P., Fishman, E., Huang, H.K. (eds.): Handbook of Medical Image Processing. San Diego, CA, USA: Academic Press 2000
178. Thompson, P.M., Vidal, C., Giedd, J.N., Gochman, P., Blumenthal, J., Nicolson, R., Toga, A.W., Rapoport, J.L.: Mapping Adolescent Brain Change Reveals Dynamic Wave of Accelerated Gray Matter Loss in Very Early–Onset Schizophrenia. Proceedings of the National Academy of Sciences of the USA 98(20), 11 650–11 655 (2001)
179. Thompson, P.M., Woods, R.P., Mega, M.S., Toga, A.W.: Mathematical/Computational Challenges in Creating Population-Based Brain Atlases. Hum. Brain Mapp. 9(2), 81–92 (2000)
180. Toga, A.W.: Brain Warping. San Diego, CA, USA: Academic Press 1998
181. Toga, A.W., Mazziotta, J.C.: Brain Mapping: The Methods. San Diego, CA, USA: Academic Press 1996
182. Toga, A.W., Thompson, P.M.: Measuring, Mapping, and Modeling Brain Structure and Function. SPIE Medical Imaging Symposium, Feb. 1997, Newport Beach, CA, USA; SPIE Lecture Notes, Vol. 3033. 1997
183. Turk, M., Pentland, A.: Eigenfaces for recognition. J. Cogn. Neurosci. 3, 71–86 (1991)
184. Turner, R., Le Bihan, D., Chesnick, A.S.: Echo-planar imaging of diffusion and perfusion. Magn. Reson. Med. 19(2), 247–53 (1991). Review
185. Vaillant, M., Davatzikos, C. Finding Parametric Representations of the Cortical Sulci Using an Active Contour Model. Med. Image Anal. 1(4), 295–315 (1997)
186. Van Essen, D.C., Drury, H.A., Joshi, S.C., Miller, M.I.: Comparisons between Human and Macaque using Shape-Based Deformation Algorithms Applied to Cortical Flat Maps. 3rd Int. Conference on Functional Mapping of the Human Brain, Copenhagen, May 19–23 1997. Neuroimage 5(4), S41 (1997)
187. Van Essen, D.C., Maunsell, J.H.R.: Hierarchical Organization an Functional Streams in the Visual Cortex. Trends Neurol. Sci. 6, 370–375 (1983)
188. Viola, P.A., Wells, W.M.: Alignment by Maximization of Mutual Information. 5th IEEE Int. Conf. on Computer Vision, pp. 16–23. Cambridge, MA, 1995
189. Wang, Y., Staib, L.: Boundary finding with correspondence using statistical shape models. Proc. Conf. Computer Vision and Pattern Recognition, pp. 338–345. Santa Barbara, CA, 1998
190. Warfield, S., Dengler, J., Zaers, J., Guttmann, C.R.G., Wells, W.M., Ettinger, G.J., Hiller, J., Kikinis, R.: Automatic Identification of Gray Matter Structures form MRI to Improve the Segmentation of White Matter Lesions. Proc. Med. Robotics & Comp. Assist. Surg (MRCAS), Nov. 4–7 1995, pp. 55–62. 1995
191. Warfield, S., Robatino, A., Dengler, J., Jolesz, F., Kikinis, R.: Nonlinear Registration and Template Driven Segmentation. In: Toga, A.W. (ed.): Brain Warping. Chapt. 4, pp. 67–84. San Diego, CA, USA: Academic Press 1998
192. Wells, W.M., Viola, P., Atsumi, H., Nakajima, S., Kikinis, R.: Multi-Modal Volume Registration by Maximization of Mutual Information. Med. Image Anal. 1(1), 35–51 (1997)
193. Witelson, S.F.: Hand and sex differences in the isthmus and genu of the human corpus callosum. A postmortem morphological study. Brain 112, 799–835 (1989)
194. Woods, R.P., Dapretto, M., Sicotte, N.L., Toga, A.W., Mazziotta, J.C.: Creation and use of a Talairach-compatible atlas for accurate, automated, nonlinear intersubject registration, and analysis of functional imaging data. Hum. Brain Mapp. 8(2–3), 73–79 (1999)
195. Woods, R.P., Grafton, S.T., Watson, J.D.G., Sicotte, N.L., Mazziotta, J.C.: Automated image registration: II. Intersubject validation of linear and nonlinear models. J. Comput. Assist. Tomogr. 22, 155–165 (1998)
196. Woods, R.P., Mazziotta, J.C., Cherry, S.R.: MRI-PET Registration with Automated Algorithm. J. Comput. Assist. Tomogr. 17, 536–546 (1993)
197. Woods, R.P., Thompson, P.M., Mazziotta, J.C., Toga, A.W.: A Definition of Average Brain Size, Orientation and Shape. 6th International Conference on Functional Mapping of the Human Brain, San Antonio, Texas, June 2000
198. Worsley, K.J., Andermann, M., Koulis, T., MacDonald, D., Evans, A.C.: Detecting changes in nonisotropic images, Hum. Brain Mapp. 8(2/3), 98–101 (1999)

199. Xu, C., Pham, D.L., Rettmann, M.E., Yu, D.N., Prince, J.L.: Reconstruction of the human cerebral cortex from magnetic resonance images. IEEE Trans. Med. Imag. 18(6), 467–480 (1999)
200. Zeineh, M.M., Engel, S.A., Thompson, P.M., Bookheimer, S.: Unfolding the Human Hippocampus with High-Resolution Structural and Functional MRI. The New Anatomist (Anat. Rec.), Apr. 15, 265(2), 111–120 (2001)
201. Zhou, Y., Thompson, P.M., Toga, A.W.: Automatic Extraction and Parametric Representations of Cortical Sulci. Comput. Graph. Applic. 19(3), 49–55 (1999)
202. Zijdenbos, A., Evans, A., Riahi, F., Sled, J., Chui, H.-C., Kollokian, V.: Automatic quantification of multiple sclerosis lesion volume using stereotactic space. Proc. 4th Vis. Biomed. Comp. (VBC), Hamburg, Germany, 1996